ACS OMEGA

http://pubs.acs.org/journal/acsodf

Article

Synthesis, Characterization, DNA/HSA Interaction, and Cytotoxic Activity of a Copper(II) Thiolate Schiff Base Complex and Its Corresponding Water-Soluble Stable Sulfinato−O Complex Containing Imidazole as a Co-ligand

Kumudini Paliwal, Paramita Haldar, P. K. Sudhadevi Antharjanam, and Manjuri Kumar*

Cite This: *ACS Omega* 2023, 8, 21948−21968

Read Online

ACCESS | Metrics & More | Article Recommendations | Supporting Information

ABSTRACT: A Cu(II) thiolato complex [CuL(*imz*)] (**1**) (H_2L = *o*-$HOC_6H_4C(H)=NC_6H_4SH$-*o*) and the corresponding water-soluble stable sulfinato−O complex [CuL′(*imz*)] (**2**) (H_2L' = *o*-$HOC_6H_4C(H)=NC_6H_4S(=O)OH$) were synthesized and characterized using physicochemical techniques. Compound **2** is found to be a dimer in the solid state as characterized using single-crystal X-ray crystallography. XPS studies clearly showed the differences in the sulfur oxidation states in **1** and **2**. Both compounds are found to be monomers in solution as revealed from their four-line X-band electron paramagnetic resonance spectra in CH_3CN at room temperature (RT). **1**−**2** were tested to assess their ability to exhibit DNA binding and cleavage activity. Spectroscopic studies and viscosity experiments suggest that **1**−**2** bind to CT-DNA through the intercalation mode having moderate binding affinity ($K_b \sim 10^4$ M^{-1}). This is further supported by molecular docking studies of complex **2** with CT-DNA. Both complexes display significant oxidative cleavage of pUC19 DNA. Complex **2** also showed hydrolytic DNA cleavage. The interaction of **1**−**2** with HSA revealed that they have strong ability to quench the intrinsic fluorescence of HSA by a static quenching mechanism ($k_q \sim 10^{13}$ M^{-1} s^{-1}). This is further complemented by Förster resonance energy transfer studies that revealed binding distances of r = 2.85 and 2.75 nm for **1** and **2**, respectively, indicating high potential for energy transfer from HSA to complex. **1**−**2** were capable of inducing conformational changes of HSA at secondary and tertiary levels as observed from synchronous and three-dimensional fluorescence spectroscopy. Molecular docking studies with **2** indicate that it forms strong hydrogen bonds with Gln221 and Arg222 located near the entrance of site-I of HSA. **1**−**2** showed potential toxicity in human cervical cancer HeLa cells, lung cancer A549 cells, and cisplatin-resistant breast cancer MDA-MB-231 cells and appeared to be most potent against HeLa cells (IC_{50} = 2.04 μM for **1** and 1.86 μM for **2**). In HeLa cells, **1**−**2** mediated cell cycle arrest in S and G2/M phases, which progressed into apoptosis. Apoptotic features seen from Hoechst and AO/PI staining, damaged cytoskeleton actin viewed from phalloidin staining, and increased caspase-3 activity upon treatment with **1**−**2** collectively suggested that they induced apoptosis in HeLa cells via caspase activation. This is further supported by western blot analysis of the protein sample extracted from HeLa cells treated with **2**.

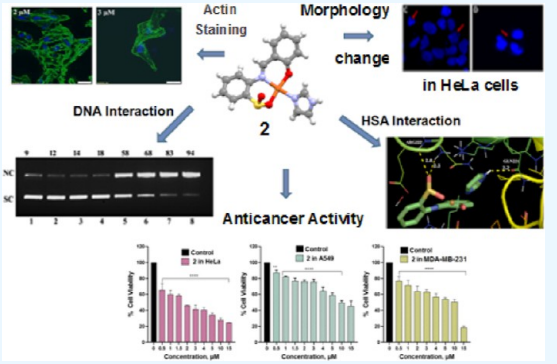

1. INTRODUCTION

Important aspects of chemistry and biochemistry of copper, a bio-essential element, as well as its role in medicinal chemistry, are well documented.[1−7] Copper(II) complexes of Schiff base and other ligands[1,2] that are able to interact with DNA as well as proteins and possess strong cytotoxic activity toward different cancer cells have been studied in order to assess their suitability as anticancer drugs.[1,2,8] Several studies were carried out for the catalytic reaction of Cu(II) with various sulfhydryl compounds.[9−13] It is well known that Cu(II) was promptly reduced by organic thiols to produce Cu(I) species and the formation of an organic disulfide. When an excess of thiol was used, Cu(I) species formed a Cu(I)-thiol complex which was readily oxidized by oxygen to Cu(II) as reported by Smith et al.[9] It is extremely difficult to directly get a Cu(II) complex coordinated with only thiol ligands. Most of the reported[1] Cu(II) complexes possessing S^- coordination are either Schiff base ligands[14−16] or mixed ligands.[17,18] In continuation of our studies[15,16] with Cu(II) compounds with Schiff base ligands derived from the reaction of pyridine-2-aldehyde or salicylaldehyde and 2-aminobenzene thiol and containing additional heterocyclic co-

Received: March 20, 2023
Accepted: May 22, 2023
Published: June 7, 2023

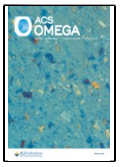

ligands like 1,10-phenanthroline (*o*-phen) or imidazole (*imz*), we have now carried out the reaction of $Cu(OAc)_2·H_2O$ and imidazole with 2-(2-hydroxyphenyl)benzothiazoline in order to get the Schiff base Cu(II) compound [CuL(*imz*)] (**1**), where H_2L = *o*-$HOC_6H_4C(H)=NC_6H_4SH$-*o*. Apart from this, we were able to synthesize the corresponding sulfinato-O-bonded copper(II) complex [CuL′(*imz*)] (**2**) (where H_2L' = *o*-$HOC_6H_4C(H)=NC_6H_4S(=O)OH$) generated in situ from aerial oxidation of **1**. It is to be noted here that there are very few reports[19,20] of Cu(II)-sulfinato−O complexes, one example is bis(2-pyridine sulfinato)copper(II) studied by Higashi et al.[19] who have synthesized this compound from the reaction of $Cu(ClO_4)_2·6H_2O$ and bis(2-pyridyl) disulfide in methanol in the presence or absence of air and studied the crystal and molecular structure of the compound. Other examples are bis-(toluene-*p*-sulfinato)copper(II) tetrahydrate and the dihydrate of bis-(benzenesulfinato)Cu(II) dihydrate complexes studied by Langs and Hare.[20] They have also reported the crystal structure of bis-(toluene-*p*-sulfinato)copper(II) tetrahydrate confirming the bonding through one of the oxygens of the sulfinato ($-SO_2$) group. Although there are many reports[1] of studying the biological activities of Cu(II) compounds containing S-donor ligands, mainly with respect to their anticancer activity, there are relatively few studies involving DNA as well as protein[21,22] interactions with compounds of Cu(II) containing sulfur-oxidized ligands bearing −SO, $-SO_2$, or $-SO_3$ groups, and it is very rare when considered for O-bonded Cu−sulfinato complexes.

Here, the synthesis, characterization, as well as biological activities of the thiolato Schiff base complex **1** and its naturally oxidized sulfinato complex **2** are reported. To the best of our knowledge, this is the first report of a water-soluble stable Cu^{II}−sulfinato complex (**2**) produced by aerial oxidation of its thiolato complex (**1**). Both **1** and **2** are found to be monomers in solution as revealed from their X-band electron paramagnetic resonance (EPR) at RT; however, **2** is found to be a dimer in solid due to the presence of axial bridging of the phenolate O^- as suggested from its X-ray crystal structure.

2. EXPERIMENTAL SECTION

2.1. Synthesis of 2-(2-Hydroxyphenyl)-benzothiazoline (A). This reported[23,24] compound was prepared and characterized as described[23] earlier from our laboratory, and details of this synthesis are given in the Supporting Information. Anal. Calcd for $C_{13}H_{11}NSO$: C, 68.09; H, 4.84; N, 6.11. Found: C, 67.82; H, 4.79; N, 6.04%.

2.2. Preparation of Cu(II) Compounds. *2.2.1. Preparation of [CuL(imz)] (1).* (H_2L = *o*-$HOC_6H_4C(H)=NC_6H_4SH$-*o*). $Cu(OAc)_2·H_2O$ (0.300 g, 0.0015 mol) and imidazole (0.204 g, 0.003 mol) were reacted in 15 mL of CH_3OH, and the dark blue reaction mixture was slowly added to a methanol (25 mL) solution of 2-(2-hydroxyphenyl)benzothiazoline[23,24] (0.342 g, 0.0015 mol) at RT (either in the presence or in the absence of air); the solution turned brown and a red-brown compound separated. After stirring for 1 h, the red-brown solid was filtered, washed well with CH_3OH, and dried. Yield ∼70%. A portion of this red-brown solid was recrystallized from degassed CH_3CN at 4 °C in a vacuum desiccator that was purged thoroughly with dinitrogen before use. Anal. Calcd for $C_{16}H_{13}N_3OSCu$: C, 53.54; H, 3.65; N, 11.71%. Found: C, 53.70; H, 3.69; N, 11.82%. ESI-MS (CH_3CN) *m*/*z*: 353.07 $[Cu_2(C_{13}H_8NOS)]^+$; *m*/*z*: 457.10 $[(o\text{-}HO\text{−}C_6H_4C(H)=N\text{−}C_6H_4\text{−}S\text{-}o)_2 + H]^+$.

2.2.2. Synthesis of [CuL(H$_2$O)] (1A). (H_2L = *o*-$HOC_6H_4C(H)=NC_6H_4SH$-*o*). 2-(2-Hydroxyphenyl)benzothiazoline (**A**) (0.228 g, 0.001 mol) was stirred in 20 mL of absolute ethanol at RT. To this, copper(II) acetate monohydrate (0.200 g, 0.001 mol) in CH_3OH (25 mL) was added dropwise, and the reaction mixture was stirred for 2 h at RT; a dark green compound separated. This was filtered, washed thoroughly with methanol followed by toluene, and then air-dried. Yield ∼90%. Anal. Calcd for $C_{13}H_{11}NO_2SCu$: C, 50.55; H, 3.59; N, 4.54%. Found: C, 51.13; H, 3.64; N, 4.63%. ESI-MS (CH_3CN) *m*/*z*: 249.05 corresponding to $[Na(C_{13}H_8NOS)]^+$; *m*/*z*: 353.07 $[Cu_2(C_{13}H_8NOS)]^+$.

2.2.3. Preparation of [CuL′(imz)] (2). (H_2L' = *o*-$HOC_6H_4C(H)=NC_6H_4S(=O)OH$). The dark green compound **1A** (77 mg, 0.00025 mol) was dissolved in 75 mL of CH_3CN and stirred; to this, 17.5 mg (0.000257 mol) of imidazole was added, the solution immediately turned brown from which a red-brown compound separated. Stirring was continued for 5 days at RT in the presence of air while the red-brown solid gradually passed into the solution that turned olive-green. This was filtered, and the olive-green filtrate was collected and kept in air for slow evaporation while an olive-green compound **2** was obtained. This was collected by filtration, rapidly washed with acetonitrile followed by toluene, and air-dried. Yield: 30 mg. This was then recrystallized from acetonitrile at RT. Anal. Calcd for $C_{16}H_{13}N_3O_3SCu$: C, 49.07; H, 3.35; N, 10.73%. Found: C, 49.38; H, 3.39; N, 10.85%. ESI-MS (CH_3CN) *m*/*z*: 391.04 $[M]^+$ corresponding to $[Cu(C_{16}H_{13}N_3O_3S)]^+$. Suitable crystals obtained from acetonitrile were used for its crystal structure.

2.3. X-ray Crystallography for 2. Single-crystal X-ray data collection (Table S1) was carried out in a Bruker D8 VENTURE dual-source single-crystal X-ray diffractometer equipped with a PHOTON 100 detector. A microfocus Cu Kα radiation source of wavelength 1.54178 Å was selected for diffraction studies. A suitable single crystal of size 0.05 × 0.10 × 0.10 mm^3 was mounted on a nylon loop with the help of Paratone-N oil. The crystal was then centered at the goniometer center with the aid of a video microscope. The automatic cell determination routine, with 20 frames (10 s exposure time/frame) at two different orientations of the detector, was employed to collect reflections for unit cell determination. The collected reflections were indexed using inbuilt Apex3 software to obtain unit cell parameters. An optimized strategy with four-fold redundancy per reflection was employed for the complete data collection by using Omega and Phi scan methods. The collected data was integrated using the Bruker Apex3/SAINT program.[25] A multiscan absorption correction was applied to the data using Bruker/SADABS.[25] The structure was solved by SHELXT[26] and refined by full-matrix least-squares techniques using SHELXL.[27] Molecular graphics were drawn using ORTEP3.[28] All hydrogens were fixed geometrically as a riding model at calculated positions with their $U_{iso}(H) = 1.2U_{eq}(C)$.

2.4. DNA Binding Experiments. *2.4.1. Absorption Spectral Studies.* UV−vis spectroscopy being an effective technique for analyzing the DNA binding ability of metal complexes, the binding experiments were performed on a Jasco V-570 UV/vis/NIR spectrophotometer using calf thymus DNA (CT-DNA). DNA stock solution was prepared using 10 mM Tris−HCl buffer (pH 7.45) by soaking overnight. The DNA-buffered solution exhibited two UV absorbance peaks at 260 and 280 nm, and the ratio A_{260}/A_{280} was found to be 1.82, indicating that the DNA was free of protein. The concentration of CT-DNA was calculated from UV absorbance at 260 nm using the

https://doi.org/10.1021/acsomega.3c01853
ACS Omega 2023, 8, 21948−21968

known molar extinction coefficient[29] ε_{260} = 6600 L mol^{-1} cm^{-1}. The DNA binding experiment was performed by keeping the concentration of the complexes (**1**−**2**) constant and adding an increasing amount of CT-DNA in 10 mM Tris−HCl buffer (pH 7.45). The reaction mixture was incubated for 2 min each time at RT before recording the spectra. Finally, the linear plot of [DNA]/($\varepsilon_a - \varepsilon_f$) vs [DNA] was used to evaluate the value of K_b, i.e., the intrinsic binding constant.

2.4.2. Viscosity Studies. Viscosity measurements using an Ostwald viscometer were conducted at RT on CT-DNA (100 μM) by varying the complex (**1**−**2**) concentration from 0 to 100 μM. Flow time was measured thrice for each sample manually using a digital stopwatch; then, an average flow time was used for calculating the viscosity ($\eta = (t - t_0)/t_0$). The flow time of buffer alone is denoted as t_0 and that with complex is denoted as t. The viscosity data was presented as $(\eta/\eta_0)^{1/3}$ against [complex]/[DNA], where η denotes the specific viscosity of CT-DNA in the presence of complexes (**1**−**2**) and η_0 represents the specific viscosity of CT-DNA alone.

2.4.3. DNA Cleavage Experiment. pUC19 DNA was employed to investigate the cleaving ability of DNA by complexes **1**−**2** with the help of gel electrophoresis. The solution of pUC19 DNA was prepared in Tris−HCl buffer containing 50 mM NaCl having pH 7.43. 200 ng of pUC19 DNA was treated with steadily increasing amounts of either **1** or **2** in order to study DNA cleavage following the oxidative pathway. Since DNA cleavage was being studied under oxidative condition, 2 μL of H_2O_2 was added in each Eppendorf tube corresponding to different lanes. The total volume in each tube was adjusted to 10 μL by adding 50 mM Tris−HCl buffer. After preparing the reaction mixtures, all Eppendorf tubes were allowed to incubate for 2 h at 37 °C. Finally, the reaction mixtures were loaded on a 1% agarose gel in 1× Tris acetic acid EDTA buffer, pH 8.4, and gel electrophoresis was carried out for 1 h 30 min at 60 V. Thereafter, 0.5 μg/mL ethidium bromide (EB) was used to stain pUC19 DNA and visualized under UV light.

Hydrolytic DNA-cleaving ability is studied without any foreign agent and light. Therefore in this experiment, to 200 ng of pUC19 DNA, only increasing amounts of either **1** or **2** (0−400 μM) were added, made up the volume to 10 μL by adding Tris−HCl, and incubated for 2 h at 37 °C, and then electrophoresis was performed in TAE for 1.5 h at 60 V, after which the gel was stained with 0.5 μg/mL EB and photographed under UV light.

Also, control experiments were performed with starting materials, $Cu(OAc)_2{\cdot}H_2O$ (400 μM), free ligand 2-(2-hydroxyphenyl)benzothiazoline (400 μM), and imidazole (400 μM) to see if they alone had any DNA cleaving ability.

2.5. HSA Binding. The fluorescence quenching measurement was done with a Jasco model FP-8500 fluorescence spectrophotometer using 1.0 cm quartz cells. To start with, 4 μM HSA solution in sodium phosphate buffer (20 mM, pH 7.4) was used to record fluorescence spectrum in the range 310−430 nm with the excitation wavelength as 295 nm. Then, with subsequent addition of the metal complex (**1**−**2**), the quenching of emission intensity was monitored. The data obtained was analyzed to get the linear Stern−Volmer plot; quenching parameters were determined using Stern−Volmer and modified Stern−Volmer equations.

Synchronous fluorescence spectral experiments were carried out using 4 μM HSA solution in sodium phosphate buffer (20 mM, pH 7.4) to which increased amounts of **1** and **2** were added. Different wavelength intervals ($\Delta\lambda$ = 15 and 60 nm) were set to observe the spectral behavior around the tyrosine (Tyr) and tryptophan (Trp) residues of HSA respectively. Here, $\Delta\lambda = \lambda_{em} - \lambda_{ex}$.

Three-dimensional (3D) fluorescence spectra were recorded by scanning the emission spectrum of 4 μM HSA alone and also in combination with 4 μM of each of the complexes **1** and **2** in the range 200−500 nm. The experiment was conducted by exciting the fluorophore at 220 nm with a successive increment of 10 nm. The excitation and emission slit opening was set as 5 nm.

Förster resonance energy transfer (FRET) calculations were done by studying the overlap between the emission spectrum of the donor fluorophore (HSA, 4 μM) and the absorption spectrum of the acceptor (complex **1**−**2**, 4 μM). The overlap integral J was determined from the plot of $\overline{I}_D(\lambda)$, normalized emission spectrum of HSA versus $\varepsilon_A(\lambda)$, and molar extinction coefficient spectrum of the acceptor complex (**1** or **2**) in the range 450−300 nm, and thereafter, it was utilized to calculate the Förster energy-transfer parameters.

2.6. Molecular Docking with DNA. The molecular structure of the B-DNA dodecamer d (CGCGAATTCGCG)2 was obtained from the Protein Data Bank (PDB ID: 1BNA). Initially, all the water molecules were removed from the B-DNA structures. Molecular dynamics simulation was performed using Gromacs 4.6.1 software.[30] Amber 99 force field was used to generate the topology file. For water solvent, the Tip4P water model was considered. Steepest descent minimization algorithm was used to perform the energy minimization phases for 100 ps. The MD simulation was performed for 1 ns using the Lincs algorithm, with Velocity Verlet algorithm and PME (particle mesh Ewald) method for long-range electrostatic interaction with a time step of 2 fs. The optimized structure of B-DNA obtained after MD simulation was used for docking studies. The partial atomic Kollman charges were added, and the .pdb file format of B-DNA was converted to .pdbqt format using Autodock Tools. Similarly, the ligand molecule (metal complex **2**) was also charged with Gasteiger−Marsili partial charges, and the .pdb file was converted to .pdbqt format. The center grid box was kept at x = 14.779, y = 20.976, and z = 8.804, and the grid box dimensions ($x \times y \times z$) were fixed to 60 × 60 × 110 Å, with a grid spacing of 0.375 Å in order to include B-DNA inside the box. The Lamarckian genetic algorithm was employed for blind docking calculations with 100 runs. The lowest energy docked conformation was selected, and PyMol software[32] (PyMol Molecular Graphic System, version 2.3.2 Schrodinger, LLC) was used to visualize the docked complex.

2.7. Molecular Docking with HSA. This is a very crucial method to interpret the molecular interaction between protein and small molecules. AutoDock Vina software[31,32] and the GROMACS 3.0 simulation package[33] were used for the molecular docking simulations and energy minimization in order to investigate the binding affinity of HSA with the Cu(II) complex **2**. During the energy minimization process, removal of water molecules followed by attachment of hydrogen atoms was initiated. MD simulation was performed having 5 × 10^5 steps for 1 ns simulation with 0.002 time step (ps/step) keeping the entire system in a canonical (NVT) ensemble[34] where the volume and number of atoms are kept unchanged with a constant temperature using a modified Berendsen thermostat. The crystallographic information file (CIF) of **2** was used. Other details are described in ref 16.

https://doi.org/10.1021/acsomega.3c01853
ACS Omega 2023, 8, 21948−21968

To characterize the interaction of complex **2** with the targeted protein molecules, PLIP, the protein−ligand interaction profiler[35] web service (https://plip-tool.biotec.tu-dresden.de) is essential. PLIP searches interactions like hydrogen bonds, hydrophobic association, π-stacking, π-cation relations, salt bridges, halogen bonds, and water bridges from the detected interaction between the protein molecule and ligands. The input file contains the final structures of the HSA−complex **2** obtained from the molecular docking study. With the input structure, the comprehensive interactions are detected by PLIP: (i) input structure preparation by hydrogenation and extraction of the metal complex along with different binding sites, (ii) characterization of functional groups of amino acids and the metal complex, (iii) matching of interacting groups of protein and metal complex using rule-based geometric criteria (distance and angle), and (iv) filtering the steps to eliminate the overlapping interaction in order to reduce the number of observed interactions. The last step is very crucial for hydrophobic interaction.

2.8. Cell Viability Assay. The MTT assay was performed on three human cancer cell lines: cervical cancer HeLa, lung cancer A549, and breast cancer MDA-MB-231. Seeded cells in a 96-well plate with a density of 2×10^4 cells per well were kept overnight in a humidified CO_2 incubator at 37 °C then treated with complexes **1** and **2** with the concentration varying from 0 to 15 μM. Upon 24 h of treatment, each well was exposed to MTT dye (0.5 mg/mL) for 4 h and kept in the dark. Thereafter, the MTT dye was removed from each well, and 100 μL of DMSO was added to dissolve the formazan crystals formed. Finally, absorbance reading was taken at 570 nm using a microplate reader. Additionally, this experiment was repeated with cisplatin using HeLa as well as MDA-MB-231 cells.

2.9. Apoptosis Assay with Hoechst Staining. HeLa cells seeded with a density of 5×10^5 in a 35 mm confocal dish were kept overnight in a CO_2 incubator at 37 °C and then after addition of 1, 2, and 3 μM concentrations of either **1** or **2** incubated for 24 h. One control dish was maintained in the same conditions for comparison. After incubation, the treated cells were washed carefully with 1× PBS, and then 4% chilled paraformaldehyde was added to each dish for fixation. Again, cells were washed with 1× PBS, and then 0.1% triton X-100 was used to permeabilize cells. After another wash with 1× PBS followed by addition of Hoechst-33342 (1 μg/mL), each dish was incubated in the dark for 30 min at RT. Following this, all dishes were washed thrice with 1× PBS and finally viewed under a fluorescence microscope (OLYMPUS CKX53).

2.10. AO/PI Dual Staining. Seeded HeLa cells (density of 5×10^5) in a 35 mm confocal dish were kept overnight in a CO_2 incubator at 37 °C, and then 1, 2, and 3 μM of either **1** or **2** were added and incubated for 24 h, while one confocal dish without adding any complex was used as a control. After 24 h of incubation, the cells were washed carefully with 1× PBS to remove media. Following this, each dish was stained with 40 μM acridine orange (AO) and 40 μM propidium iodide (PI) and kept in the dark for half an hour at 37 °C, washed using 1× PBS (once), and finally viewed under a fluorescence microscope.

2.11. Caspase-3 Activity Assay. The colorimetric caspase-3 assay kit (ab39401) obtained from Abcam was employed to assess caspase-3 activation. To begin with, 1×10^6 HeLa cells seeded in a 90 mm Petri dish were left for attachment in a humidified CO_2 incubator at 37 °C, three doses (1, 2, and 3 μM) of either **1** or **2** were added and incubated for 24 h. These cells were collected and resuspended in 50 μL of lysis buffer for 10 min in ice. The supernatant was collected, and protein concentration was measured using Bradford. The protein concentration of 1 μg/μL was used in all samples. Next, the cell lysate was added to the 50 μL reaction buffer that contained 10 mM DTT and 5 μL of the 4 mM DEVD-pNA substrate and incubated for 2 h at 37 °C. Finally, absorbance was measured at 405 nm using a microplate reader.

2.12. Western Blot Experiment. In order to perform western blot analysis, HeLa cells were treated with three different concentrations (1, 2, and 3 μM) of complex **2**, and protein was extracted with RIPA lysis buffer after 24 h of incubation with compound **2**. The concentration of the extracted protein was determined by the Bradford reagent. The protein concentration of 60 μg per well was used during SDS−PAGE. Following a 2 h transfer to the PVDF membrane, the membrane was incubated with primary antibodies overnight at 4 °C. All antibodies, namely, rabbit β-actin (mAb 4970), rabbit cleaved caspase-8 (mAb 9496), and rabbit cleaved caspase-9 (mAb 7237) purchased from Cell Signaling Technology, were used with 1:1000 dilution. The following day, the membrane was washed with IX TBST, five times for 5 min. The incubation time for goat antirabbit secondary antibody (dilution 1:3000) was 2 h at RT, followed by washing with IX TBST five times for 5 min. Finally, blot images were developed on a X-ray film in the dark room with the help of ECL reagents.

2.13. Phalloidin Staining. Seeded HeLa cells ($\sim 5 \times 10^5$) in a confocal dish were kept overnight in a humidified CO_2 incubator; these were then exposed to three concentrations (1, 2, and 3 μM) of complexes **1**−**2**. After 24 h of incubation, these cells were fixed by using 4% paraformaldehyde for 10 min, followed by permeabilization by 0.1% Triton X 100 for 10 min. The fixed cells were then stained by using 400 μL of Phalloidin (Phalloidin-iFluor 488) and 400 μL of Hoechst 33342 for 30 min in the dark. Following this incubation, the cells were washed three times with 1× PBS and then visualized under a confocal microscope at 100×.

2.14. DNA Content/Cell Cycle Analysis. To understand the effect of **1**−**2** on cell cycle progression of HeLa cervical cancer cells, cell cycle analysis was done using flow cytometry. HeLa cells were seeded with a density of 5×10^5 cells into a 35 mm confocal dish. After 24 h, except one control dish left untreated, all others were treated with three different amounts of either **1** or **2**. Following 24 h of incubation, these cells were trypsinized, centrifuged, and fixed with 70% ethanol for half an hour with regular vortexing. Further, after adding 10 μg of RNase to each sample, these were incubated at 37 °C for 30 min. PI (50 μg/mL) was then added to each sample, kept in ice (4 °C) for 30 min in the dark, and then transferred to FACS tubes for analysis using BD FACS Melody.

3. RESULTS AND DISCUSSION

3.1. Synthesis and Characterization. 2-(2-Hydroxyphenyl)benzothiazoline (A, Scheme 1) undergoes rearrangement in solution in the presence of a metal ion to the corresponding Schiff base (B, Scheme 1) that coordinates to the metal ion as a tridentate S^-NO^- Schiff base ligand.[16,23,24] It is to be noted here that there will be an equilibrium between A and B (Scheme 1) in solution, and the metal ion present in the solution usually coordinates to the deprotonated form of B that acts as a tridentate dianionic Schiff base, thereby shifting the equilibrium toward B and thus forming the Schiff base complex. However, there is evidence that apart from the coordination of B as a dianionic tridentate Schiff base, the cyclized form A was also

https://doi.org/10.1021/acsomega.3c01853
ACS Omega 2023, 8, 21948−21968

Scheme 1. Proposed Structures of the Reactants and the Products Involved in Synthesis; 2-(2-hydroxyphenyl)benzothiazoline (A), In Situ Rearrangement to Schiff Base (B) in Solution, Red-Brown Complex 1 Formed after Reaction with $Cu(OAc)_2{\cdot}H_2O$ and Imidazole in Methanol in the Presence of Air, Dark Green Cu^{2+} Complex 1A Isolated from the Coordination of Deprotonated B as the $S{-}NO^-$ Donor, Imidazole Complex 1 Formed on the Reaction of Imidazole with 1A in CH_3OH without Thiol Oxidation, and O-Bonded Sulfinato Complex 2 Formed from Aerial Oxidation of 1 either in CH_3CN or in Ethanol

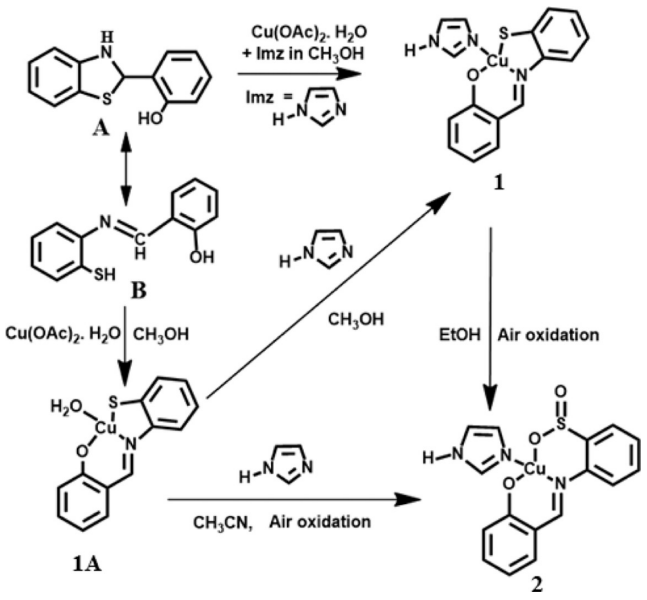

found to coordinate to the same metal ion as a monoanionic monodentate ligand as reported[24] by Fandos and co-workers for a titanium complex that was prepared from the reaction of $[TiCp^*Me_3]$ (where $Cp^* = \eta^5\text{-}C_5Me_5$) with 2-(salicylideneamino)thiophenol in a 1:2 M ratio. However, when a mixture of $Cu(OAc)_2{\cdot}H_2O$ and imidazole (1:2) in methanol was reacted with A, either in the presence or absence of air, a red-brown compound was isolated from the solution owing to its very low solubility in methanol. This red-brown compound was found to contain the tridentate S^-NO^- Schiff base ligand along with the imidazole as a fourth ligand forming the square-planar complex **1**, [CuL(*imz*)] (Scheme 1) (where H_2L = *o*-HO−C_6H_4C(H)=N−C_6H_4−SH-*o*).[23,24] On the other hand, when $Cu(OAc)_2{\cdot}H_2O$ in methanol was reacted with only 2-(2-hydroxyphenyl)-benzothiazoline in ethanol/methanol in the presence of air, a dark green compound was isolated that was found to contain Cu^{2+} coordinated with the tridentate S^-NO^- Schiff base ligand and an aqua ligand forming the four-coordinate complex [CuL(H_2O)] (**1A**, Scheme 1). This dark green compound **1A** is possibly a dimer in solid due to axial bridging of the phenolate O^- as observed in compound **2**, or it could be due to S bridging as reported by Moosun et al.[36] for a dark green compound of Cu(II) that was prepared with the ligand *N*,*N*′-(1,1′-dithio-bis(phenylene))-bis-(salicylideneimine) where S acted as a bridging ligand. Moreover, **1A** readily reacts with imidazole in methanol in the presence of air resulting in the same red-brown compound [CuL(*imz*)] (**1**) that was immediately separated from the solution. However, when the dark green compound [CuL-(H_2O)] (**1A**) was reacted with imidazole in acetonitrile and the solution was stirred at RT in the presence of air for 4/5 days, it resulted in a olive-green solution from which the O-bonded sulfinato complex **2**, [CuL′(*imz*)] Scheme 1 (H_2L' = *o*-$HOC_6H_4C(H){=}NC_6H_4S(=O)OH$), was isolated upon evaporation of the solvent. It is to be noted that though **1A** also immediately produced **1** upon reacting with imidazole in CH_3CN as evident from color change from dark green to red brown, but **1** having much better solubility in CH_3CN than CH_3OH, it slowly reacts with oxygen in air to yield **2** having high solubility in CH_3CN, resulting in an olive-green solution. Thus, the red-brown compound **1** gradually passes into the CH_3CN solution due to its in situ aerial oxidation and conversion to the more soluble olive-green compound **2** from which the latter was isolated. Compound **2** may also be obtained from the ethanol solution of **1** (Scheme 1) on standing at RT in the presence of air for a few days; however, the yield is low because of low solubility of **1** in ethanol. It is to be noted that though the aerial oxidation in solution is very slow, the conversion is found to be quantitative as revealed from their respective electronic spectra in ethanol or in acetonitrile. The solubility of compound **2** is found to be good in methanol, ethanol, and water. **2** is a monomer in solution as revealed from its mass as well as X-band EPR spectra in CH_3CN solution at RT (vide infra). The presence of the oxidized sulfinato ligand in **2** was suggested from its XPS spectra and its coordination as O^-NO^- to the Cu^{2+} ion was confirmed from its crystal structure (Figure 1).

It is to be noted here that there are reports[37−39] of a few Fe(III) sulfinato complexes with remarkable properties or catalytic activities. Wu et al.[37] have reported a low-spin bisthiolate Fe^{III} complex that yielded mixed sulfinate/thiolate and O-bound bis-sulfinate species upon S-oxygenation. They also observed the hydration of the C=N bond by HO^- in the monosulfinate species due to more polarization of the Fe-bound imine bonds (C=N) in the monosulfinate species. Cavell et al.[38] have reported a O-bonded sulfinato Fe(III) complex containing a seven-membered chelate ring that was found to be highly efficient in electrocatalytic proton reduction. Another Fe(III) compound $(Et_4N)[Fe^{III}(PyPS)]$, which was five coordinate with one pyridine nitrogen, two deprotonated carboxamido nitrogens, and two thiolato S^- donors and having a trigonal bipyramid structure that was designed[39] to mimic the iron(III) site of Fe-containing nitrile hydratase, was found to be converted on exposure with a limited amount of dioxygen to *bis*-sulfinic species, and the more stable O-bonded sulfinato complex $(Et_4N)[Fe^{III}(PyP\{SO_2\}_2)]$ was structurally characterized. Apart from these, there were reports[40−42] of other thiolato complexes that underwent S-oxidation, leading to the formation of either S-bonded or O-bonded sulfinato complexes, or sometimes both S-bonded and O-bonded sulfinato complexes were also formed.

3.2. UHPLC. ESI-MS (positive ion mode) for **1** in CH_3CN showed peaks (Figure S1A,B, Supporting Information) at *m*/*z* 353.07 corresponding to $[Cu_2(C_{13}H_8NOS)]^+$ and at *m*/*z* 457.10 corresponding to $[(o\text{-}HO{-}C_6H_4C(H){=}N{-}C_6H_4{-}S\text{-}o)_2 + H]^+$. Compound **1A** in CH_3CN exhibited peaks (Figure S2A,B, Supporting Information) at *m*/*z* 249.05 corresponding to $[Na(C_{13}H_8NOS)]^+$, where $C_{13}H_8NOS$ is the deprotonated form of 2-(2-hydroxyphenyl)benzothiazole, the oxidized species of the free ligand 2-(2-hydroxyphenyl)benzothiazoline, and at *m*/*z* 353.07 corresponding to $[Cu_2(C_{13}H_8NOS)]^+$. The green compound **2** in CH_3CN, on the other hand, showed a peak at *m*/*z* 391.04 $[M]^+$ (Figure S3, Supporting Information) correspond-

https://doi.org/10.1021/acsomega.3c01853
ACS Omega 2023, 8, 21948−21968

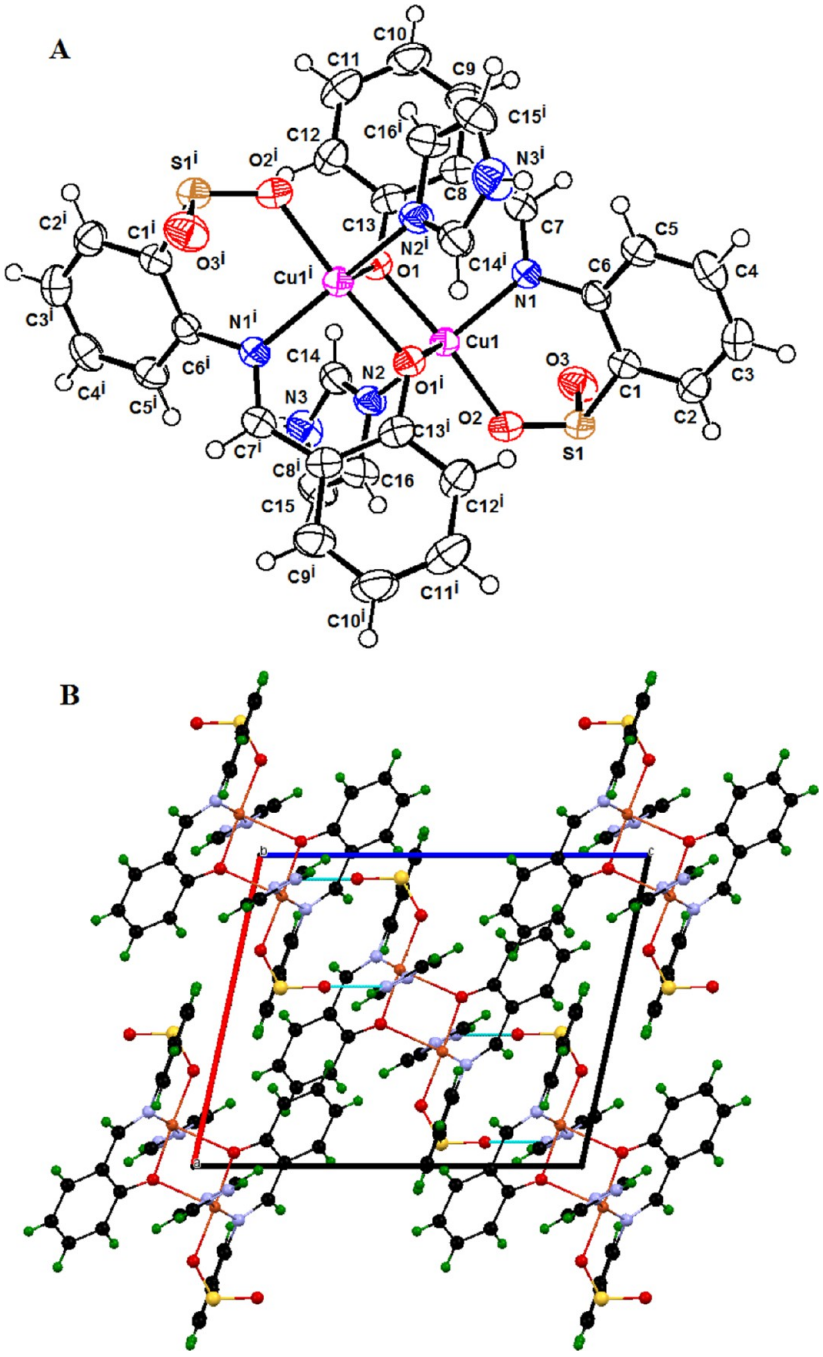

Figure 1. Molecular structure of **2**: (A) ORTEP (50%) diagram. (B) Unit cell packing of the molecules.

ing to $[Cu(C_{16}H_{13}N_3O_3S)]^+$, suggesting the presence of the sulfinato ligand in compound **2**.

3.3. XPS Results. Binding energy shifts (ΔE's) were calculated by taking the E^0 values for Cu($2p_{3/2}$), S($2p_{3/2}$), N(1s), and C(1s) as 932.6 eV, 164.0, 401.6, and 284.8 eV, respectively.[43−46]

The XPS data clearly reveals the influence of sulfur oxidation states on the S($2p_{3/2}$) binding energies for the complexes **1**, **1A**, and **2**. While it is close for **1** and **1A** as expected for the thiol coordination in both, it is quite different for **2**. While the S($2p_{3/2}$) peak for **1** is observed at 161.4 eV (ΔE = −2.6 eV) and that for **1A** is observed at 162.2 eV (ΔE = −1.8 eV), this peak was observed at 167.8 eV (ΔE = 3.8 eV) for **2** (Figure S4), and no peak for **2** was observed in the region 160−165 eV, clearly suggesting complete oxidation of thiolate sulfur to sulfinato in the aerial oxidation of **1** to produce **2**. As expected, only one XPS peak was observed for N(1s) for **1A** (398.98 eV and ΔE = −2.62 eV), while at least two XPS peaks were observed for both **1** (398.88 and 399.89 eV) and **2** (399.25 and 400.44 eV) due to the presence of the imine nitrogen of the Schiff base as well as the nitrogens of the imidazole co-ligand. Apart from these, marked differences are also observed for the O(1s) spectra. For **1**, the O(1s) peak appeared at 530.45 eV, and for **1A**, this peak was seen at 530.60 eV with a distinct shoulder at 532.64 eV, while these are significantly different in **2** (peak at 531.62 eV, sh at 533.22 eV) due to the presence of sulfinato O atoms. There is no significant difference in C(1s) peaks for **1** (peak at 284.12 eV, sh at 285.08 eV), **1A** (peak at 284.29, sh 285.08 eV), and **2** (peak at

https://doi.org/10.1021/acsomega.3c01853
ACS Omega 2023, 8, 21948−21968

284.66, sh 285.63 eV). However, Cu($2p_{3/2}$) peaks for **1** (933.5 eV and ΔE = 0.9 eV) and **1A** (933.0 eV and ΔE = 0.4 eV) are found to be lower than that for **2** (934.6 eV and ΔE = 2.0 eV), suggesting less electron density on Cu^{2+} in **2** as compared to **1** and **1A**, owing to the difference in their coordination, mainly due to sulfinato O^- in **2** versus thiolato S^- in **1** and **1A**.

3.4. Infrared Spectra. The ν(N−H) stretching[23] observed at 3252 cm^{-1} (figure not shown) for 2-(2-hydroxyphenyl)-benzothiazoline (**A**) is not observed in the IR spectra of **1** and **2** (Figure S5), suggesting its rearrangement[16,23] to produce in situ the Schiff base complex and the N of the C═N, thiolate S^-, and phenolate O^- coordinate to the metal ion. **1** exhibited ν(C═N) at 1608 cm^{-1}, ν(C═N) for **2** was observed at 1603 cm^{-1}, while **1A** exhibited ν(C═N) at 1607 cm^{-1} (Figure S6). A broad peak centered around 3657 cm^{-1} was observed in the IR spectrum of **1A**, indicating the presence of water molecules in this compound. ν_{as}(S−O) and ν_s(S−O) bands appeared at 1014 and 962 cm^{-1} as a medium and weak peak, respectively, in the IR spectrum of complex **2**. These latter two bands are absent in the IR spectra of **1** and **1A**. It is to be noted here that ν_{as}(S−O) and ν_s(S−O) bands for the reported[19] O-bonded bis(2-pyridine sulfinato)copper(II) complex were observed at 1040 and 930 cm^{-1}, respectively, while those for [Cu(*p*-$MeC_6H_4SO_2)_2(H_2O)_4$] were found[20] at 998 and 938 cm^{-1}, respectively. The presence of O-bonded sulfinato ligand in **2** is confirmed from X-ray crystallography.

3.5. Electronic Spectra. The electronic spectra of **1** and **2** in CH_3CN are displayed in Figure S7. The red-brown solution of compound **1** in acetonitrile showed a weak broad band centered around 575 nm arising due to ligand field transition; charge-transfer (CT) transitions were observed in the 450−200 nm region (Figure S7, Supporting Information). The green solution of **2** in acetonitrile displayed a broad band centered around 670 nm, while CT bands were observed in the 400−200 nm region. The differences in their electronic structures are clearly seen from their electronic spectra (Figure S7). The CH_3CN solution of **1A**, on the other hand, displayed a weak broad band centered at ∼630 nm originating from ligand field transition, while three strong charge-transfer bands (Figure S8) were observed at 400, 289, and 220 nm, respectively, for this compound.

Compound **1** is not soluble in water, so it was dissolved in a minimum volume of DMSO and then diluted with respective buffer for carrying out the biological experiments. Before that, the stability of compound **1** in Tris−HCl buffer as well as in DMEM was checked by monitoring the electronic spectra of these solutions with time. **1** was found to be quite stable in both the solutions (Figure S9). On the other hand, compound **2** was found to be soluble in water, and the green water solution was found to be highly stable as shown in Figure S10. Also, the electronic spectra of **2** in water and in Tris−HCl buffer are found to be very similar (Figure S11). All experiments were carried out using fresh solutions of the compounds.

3.6. EPR Spectra. Compounds **1** and **2** showed strong X-band EPR (Figures S12 and S13) in the powder state, suggesting that they are paramagnetic. The *g* values calculated for **1** from its powder spectra are $g_\parallel$ = 2.144 and $g_\perp$ = 2.067 at RT and $g_\parallel$ = 2.120 and $g_\perp$ = 2.057 at LNT. The four-line spectrum ($^{63/65}$Cu nucleus, I = 3/2) displayed by **1** in acetonitrile at RT (Figure S12) suggested that it is a monomer in solution (g_{iso} = 2.078 and A_{iso} ∼ 8 mT). **1** in CH_3CN at LNT displayed a characteristic monomeric spectrum having $g_\parallel$ = 2.157, $g_\perp$ = 2.052; $A_\parallel \approx$ 18.0 mT and $A_\perp \leq$ 5.9 mT, respectively.

Compound **2** displayed an isotropic signal (Figure S13A) in its powder state with its g = 2.084 for **2**. This compound also exhibited a four-line EPR multiplet in acetonitrile at RT (Figure S13B), revealing that it is monomer in solution. g_{iso} for **2** was 2.104, while A_{iso} was ∼7 mT.

3.7. Cyclic Voltammetry. The redox properties of **1** and **2** were studied using CV in CH_3CN at RT using 0.1 M [N(*n*-$Bu)_4$]ClO_4 as the supporting electrolyte in a dinitrogen atmosphere (Figure S14, Supporting Information). Starting with an initial negative scan from 0.0 V, a reduction wave was observed at −0.88 V for **1**. Broad oxidation waves were seen at +0.75 and +1.15 V, respectively, on scan reversal. Another scan reversal did not show any reductive response within 0.0 V (Figure S14A). No corresponding anodic or cathodic responses were observed, suggesting that this compound undergoes an irreversible electrochemical process. The cathodic peak at −0.88 V is most likely associated with an irreversible Cu(II)/Cu(I) redox process. For compound **2**, a broad reduction wave was observed at −0.49 V with an initial negative scan; no corresponding oxidation wave was detected on scan reversal (Figure S14B). This compound was found to undergo irreversible oxidation as evident from the broad oxidation wave centered around +1.29 V; no corresponding reduction wave was seen on scan reversal, and this oxidation wave was observed for both negative and positive scan directions.

3.8. X-ray Crystal Structure of 2. The molecule crystallized in a monoclinic primitive unit cell with the space group $P2_1/n$. The asymmetric unit contains half of the given complex, the binuclear complex is formed by joining its inversion equivalent, and central copper atom is being penta-coordinated with the tridentate ligand and imidazole moieties (Figure 1A). The geometry index value, known as tau (τ)[47] ($\tau = (\beta - \alpha)/60$, β and α being the largest basal angles), of the copper complex is found to be $(174.04 - 162.98)/60 = 0.18$, suggesting a distorted square pyramidal environment for the central copper ion in the complex with the basal plane formed by O1, O2, N1, and N2 and the apex was formed by the inversion equivalent of O1 ($-x + 1$, $-y + 1$, and $-z + 1$). Important bond lengths and bond angles for complex **2** are tabulated in Table 1. The oxygen atom O1 of the ligand (phenolate O^-) acts as a bridge in joining the two copper centers. Figure 1B shows the unit cell with packing of the molecules. The molecules in the lattice are held together by N(3)−H(3A)···O(3) hydrogen bond interaction with a d(H···

Table 1. Selected Bond Distances and Bond Angles for the Copper Complex 2

bond distances (Å)		coordination angles (deg)	
Cu(1)−O(1)	1.921(2)	O(1)−Cu(1)−O(2)	174.04(11)
Cu(1)−O(2)	1.955(3)	N(1)−Cu(1)−N(2)	162.98(12)
Cu(1)−N(1)	2.000(3)	O(1)−Cu(1)−N(1)	91.60(11)
Cu(1)−N(2)	2.004(3)	O(2)−Cu(1)−N(1)	94.33(11)
Cu(1)−O(1)#1	2.355(3)	O(1)−Cu(1)−N(2)	87.68(11)
		O(2)−Cu(1)−N(2)	86.49(11)
		O(1)−Cu(1)−O(1)#1	84.60(10)
		O(2)−Cu(1)−O(1)#1	95.01(11)
		N(1)−Cu(1)−O(1)#1	98.76(10)
		N(2)−Cu(1)−O(1)#1	98.10(11)

#1 = ($-x + 1$, $-y + 1$, $-z + 1$)

https://doi.org/10.1021/acsomega.3c01853
ACS Omega 2023, 8, 21948−21968

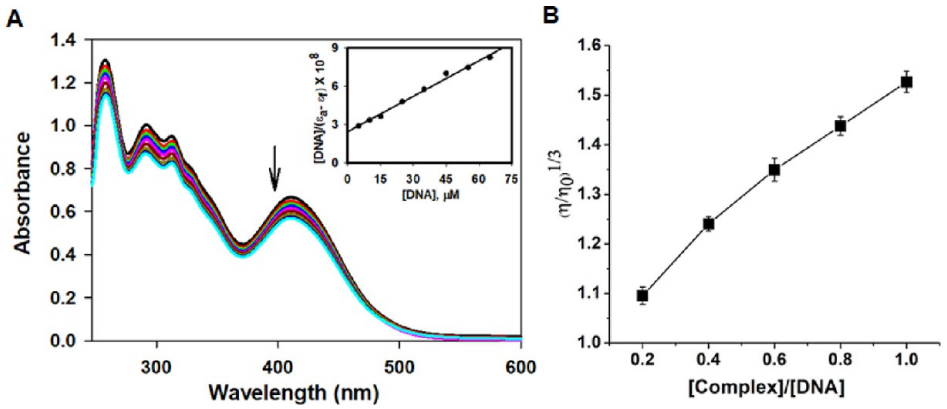

Figure 2. (A) Changes in the absorbance spectra of **1** (1×10^{-4} M) in Tris−HCl solution (pH 7.4), with increasing concentration of CT-DNA (0−65 μM). Plot of [DNA]/($\varepsilon_a - \varepsilon_f$) versus [DNA] shown in the inset (R^2 = 0.98979 for eight points). (B) Effects on viscosity of CT-DNA in 10 mM Tris−HCl (pH 7.4) with increasing concentration of complex **1**: plot of relative specific viscosity against [complex]/[DNA], where [CT-DNA] is 100 μM and [complex] = 0 to 100 μM.

A) distance of 1.98(2) Å (<DHA = 152.7(3). Figure S15A shows N−H···O and C−H···O interactions, and hydrogen bond parameters for **2** [Å and °] are given in Table S2. Apart from this, the crystal lattice is also stabilized by CH···S, CH···O, and CH···π interactions (Table S3 and Figure S15B).

3.9. DNA Binding Studies. *3.9.1. Electronic Absorption Spectral Titration.* Electronic spectroscopy is one among the useful techniques used to study DNA binding, as the mode of interaction is indicated from the observed spectral changes.[48−50] Therefore, interactions of **1** and **2** with CT-DNA in Tris−HCl buffer (10 mM) having pH 7.4 were studied by employing UV−vis electronic absorption spectroscopy at RT. Figure 2A shows the absorption spectral change of complex **1** with the addition of increasing amount of CT-DNA. The absorption spectra of **2** with increasing CT-DNA concentration is shown in Figure S12A. As can be seen from the spectroscopic titrations (Figures 2A and S16A), increased amounts of DNA led to a decrease in absorption intensity (hypochromism). Generally, hypochromism is considered to arise owing to the intercalative mode of DNA binding that is resulted from strong stacking of an aromatic chromophore into DNA base pairs.[49] The intrinsic binding constant K_b was determined using the Wolfe−Shimer equation[51] (eq 1).

$$\frac{[\mathrm{DNA}]}{(\varepsilon_a - \varepsilon_f)} = \frac{[\mathrm{DNA}]}{(\varepsilon_b - \varepsilon_f)} + \frac{1}{K_b(\varepsilon_b - \varepsilon_f)} \quad (1)$$

where [DNA] denotes the concentration of CT-DNA used and ε_f, ε_a, and ε_b denote the free, apparent, and bound metal complex extinction coefficients, respectively.

The K_b values for complexes **1**−**2** determined from the ratio of slope to intercept of the plots of [DNA]/($\varepsilon_a - \varepsilon_f$) versus [DNA] were found to be in the range 3.03×10^4 to 3.78×10^4 M^{-1}. For reported classical intercalator EB,[52] $K_b = 3.3 \times 10^5$ M^{-1} in 50 mM Tris−HCl/1.0 NaCl buffer, pH 7.5. Thus, the observed K_b values for complexes **1**−**2** under study were found to be lower than that of a typical classical intercalator EB,[52] which means that **1** and **2** bind to CT-DNA with an affinity less than that of the classical intercalator.

3.9.2. Viscosity Measurement. Although spectroscopic data is essential, it is insufficient to ascertain an intercalative mode of DNA binding. Hydrodynamic methods such as sedimentation or viscosity studies which are sensitive to length increase are considered to be confirmatory experiments to specify the binding mode.[53] In the case of intercalation mode, a significant rise in the viscosity of DNA solution is observed due to intercalation of a ligand into DNA base pairs that results in local unwinding of the DNA helix and hence increases the overall contour length, while classical groove binders have no effect on DNA length; thus, there is no impact on solution viscosity.[49] In the case of partial intercalators that can bend or kink the DNA helix thus reducing its length subsequently results in lowering its viscosity.[49] The effect of **1** and **2** on the viscosity of CT-DNA at RT has been studied, and relative specific viscosity $(\eta/\eta_0)^{1/3}$ versus [complex]/[DNA] has been plotted, and a sequential increase in viscosity has been noticed (Figures 2B and S16B), which confirms that **1** and **2** bind to CT-DNA through the intercalative mode as it was already indicated from spectroscopic analysis.

3.9.3. DNA Cleavage Studies. The DNA cleavage ability of **1**−**2** was examined by gel electrophoresis that determines conversion of supercoiled circular (SC) form of DNA into nicked circular (NC) form and linear form. In electrophoresis, the fastest migration is observed for supercoiled form (form I). When one strand of DNA is cleaved, the DNA supercoils are relaxed to generate a slower moving NC form (form II),[54] while cleavage of both DNA strands results in a linear form (form III), which migrates[55−57] in between SC and NC forms. Metal complexes can cleave nucleic acids via both oxidative and hydrolytic pathways.[54] Oxidative cleavage requires the addition of external agents like oxidative or reductive species and light to initiate the cleavage process. During oxidative DNA cleavage, reactive oxygen species (ROS) such as hydroxyl radical, singlet oxygen, and superoxide species are formed, which damages the ribose sugar and/or nucleic bases of the DNA.[58,59] In contrast, hydrolytic cleavage requires hydrolysis of the phosphodiester linkages of DNA and is studied in the absence of any foreign agent and light. An important factor in hydrolytic DNA cleavage is that the diester bond in DNA is extremely strong (for unhydrolyzed ds-DNA, the rate constant $k = 3.6 \times 10^{-8}$ h^{-1});[16] it requires nucleophilic activation that causes high enhancement in hydrolysis rate. Thus, compounds that are capable of causing hydrolytic DNA cleavage under physiological conditions are of extreme importance in enzymatic catalysis and drug design technology.

In oxidative DNA cleavage experiment, the electrophoretic separation of pUC19 DNA induced upon treatment with various concentrations of **1** in the presence of H_2O_2 as an oxidizing agent

https://doi.org/10.1021/acsomega.3c01853
ACS Omega 2023, 8, 21948−21968

is shown in Figure 3A (lanes 1−7). As can be seen from the figure, complex **1** could cleave plasmid DNA from form I to form

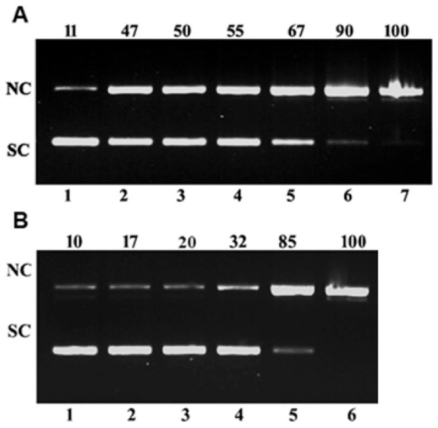

Figure 3. Agarose gel electrophoresis (A) showing concentration-dependent oxidative cleavage of 200 ng pUC19 DNA by complex **1** at 37 °C in Tris−HCl (50 mM, pH 8). Lane 1, control: only pUC19 DNA; lanes 2−7, complex **1** (5, 10, 25, 50, 100, and 200 μM) + H_2O_2 (1 mM). (B) Oxidative cleavage of 200 ng pUC19 DNA by complex **2** at 37 °C in 50 mM Tris−HCl having pH 8. Lane 1, control: only pUC19 DNA; lanes 2−6, complex **2** (2.5, 5, 10, 25, and 50 μM) + H_2O_2 (1 mM).

II, indicating that it is capable of single-strand scission. A complete 100% conversion of DNA from form I to form II was seen at 200 μM dose of **1** (Figure 3A, lane 7); thus, it is evident that **1** exhibited considerable cleavage in the presence of H_2O_2. Also, the cleavage experiment in the presence of H_2O_2 was done with complex **2**. As can be seen in Figure 3B (lanes 1−6), the intensity of the supercoiled SC (form I) DNA slowly decreased with increasing amount of **2** and fully converted to nicked form (NC) at 50 μM dose of complex **2** (Figure 3B, lane 6), indicating that it is far more effective in cleaving DNA oxidatively as compared to complex **1**.

Hydrolytic cleavage experiment without any foreign reagent or light was also carried out with **1**−**2** to assess their capabilities for hydrolytic DNA cleavage. **1** did not show any appreciable cleavage, indicating that it is not capable of causing any hydrolytic DNA cleavage (Figure S17); however, complex **2** was found to cleave DNA hydrolytically (Figure 4). At 100 μM

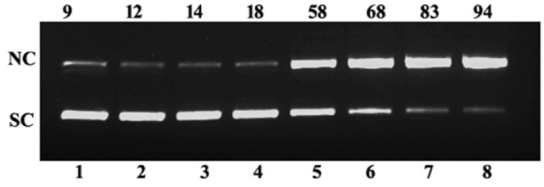

Figure 4. Agarose gel electrophoresis showing hydrolytic cleavage of 200 ng pUC19 DNA by complex **2** in 50 mM Tris−HCl having pH 8 at temperature 37 °C. Lane 1, pUC19 DNA control; lanes 2−8, complex **2** (10, 25, 50, 100, 200, 300, and 400 μM).

concentration and with 2 h incubation, appreciable conversion (58%) and eventually at 400 μM dose almost complete conversion to NC form were observed (Figure 4, lane 8). Thus, from the above studies, we may infer that complex **2** being able to cleave DNA following both oxidative and hydrolytic pathways is a better DNA cleaving agent than complex **1**.

Also, cleavage experiments were done with $Cu(OAc)_2{\cdot}H_2O$ (400 μM) and free ligands 2-(2-hydroxyphenyl)benzothiazoline (400 μM) and imidazole (400 μM) to establish complexes **1**−**2** as a whole were responsible for bringing about DNA cleavage. No cleavage was detected with either $Cu(OAc)_2{\cdot}H_2O$, or either of the free ligands even at a high concentration of 400 μM. These observations confirm that none of the starting materials are capable of causing any DNA cleavage, but complexes **1**−**2** as a whole are effective in cleaving DNA.

3.10. HSA Interaction Studies. *3.10.1. Fluorescence Quenching Studies.* HSA is the most abundant protein in the circulation system and capable of binding small molecules and drugs and therefore plays a prominent role in the transfer of several types of drugs through the bloodstream to the sites of the disease.[21,22,60−63] Also, HSA shows a relatively high uptake in tumor tissues; hence, its ability to accumulate in tumors makes HSA an effective tool for drug delivery in anticancer-related studies.[21] Thus, drug binding to serum albumin like HSA is a crucial factor that improves the drug efficacy and delivery to the target site. The structural arrangement of HSA is such that it allows a number of ligand binding sites. HSA has three domain structures with two high affinity binding sites for heterocyclic or aromatic molecules in subdomains IIA and IIIA.[64,65] Quantitative analysis of the binding interaction between copper(II) complex (**1** or **2**) with HSA was performed by fluorometric titration. HSA fluorescence is mainly due to Trp and Tyr residues; however, when excitation is at 295 nm, only the Trp residue gets excited.[70] In our study, 4 μM solution of HSA was titrated with increasing concentration of complexes **1**−**2**, and the fluorescence spectra were monitored in the 300−440 nm region upon excitation at 295 nm (Figure 5). The broad characteristic band of HSA (λ_{max} = 345 nm) was highly quenched with increasing amounts of **1** and **2**, which indicates the existence of significant interaction between HSA and the complex, causing a change in the local environment of the hydrophobic regions of HSA around the Trp residue. In the case of complex **2**, fluorescence quenching of HSA was accompanied by a noticeable amount of red shift (14 nm) in the emission maxima (Figure 5B). No such shift was observed in the case of complex **1** (Figure 5A), thus indicating that the binding site of complex **1** on HSA may be different from that of complex **2**.

The fluorescence quenching is given below by the Stern−Volmer eq 2.

$$\frac{F_0}{F} = 1 + K_{SV}[Q] = 1 + k_q\tau_0[Q] \quad (2)$$

Here, [Q] is the quencher or complex concentration and τ_0 is the average lifetime of HSA without any quencher and is taken as 5.71×10^{-9} s. F_0 and F are respective fluorescence intensities without and with a quencher. After analysis of fluorescence data obtained from the interaction of **1** and **2** with HSA, the linear Stern−Volmer plot was generated (inset of Figure 5), and the constant K_{sv} was calculated from this F_0/F against [Q] plot and is presented in Table 2. It is known that for a dynamic quenching approach, the maximum collision quenching constant has a value of 2.0×10^{10} M^{-1} s^{-1}. The bimolecular quenching constant k_q evaluated using eq 2 in the present study is in the order of 10^{13} M^{-1} s^{-1} (Table 2) for complexes **1**−**2**, which is much higher than the highest attainable bimolecular quenching constant value reported for a dynamic quenching, thus suggesting that complexes **1**−**2** suppress HSA fluorescence in a static rather than a dynamic manner.

To understand the quenching effect in more detail, fluorescence quenching data was also analyzed using the modified Stern−Volmer equation (eq 3), and the linear double

https://doi.org/10.1021/acsomega.3c01853
ACS Omega 2023, 8, 21948−21968

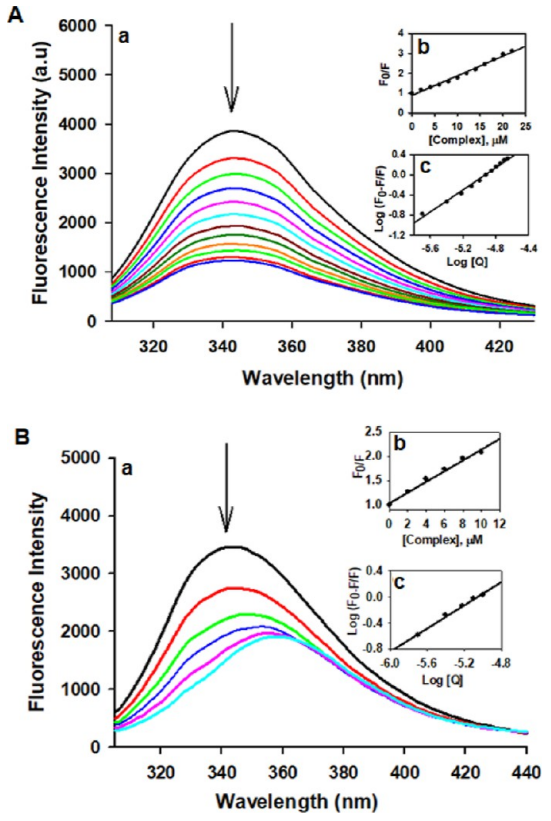

Figure 5. Fluorescence emission spectra of HSA (4 μM) in sodium phosphate buffer (20 mM, pH 7.4). Black curve denotes the emission intensity without complex. Quenching of fluorescence with an increase in compound concentration is indicated by an arrow. Panel (A): (a) shows quenching with increasing concentration of **1**, (b) Stern–Volmer plot (R^2 = 0.9875 for 11 points), and (c) modified Stern–Volmer plots shown in the inset (R^2 = 0.9885 for 11 points). Panel (B): (a) shows quenching with increasing concentration of **2**, (b) Stern–Volmer plot (R^2 = 0.99597 for 5 points), and (c) modified Stern–Volmer plots shown in the inset (R^2 = 0.99126 for 5 points).

Table 2. Binding Parameters Derived from Fluorescence Quenching

system	K_{sv} (M^{-1})	k_q (M^{-1} s^{-1})	n	K_a (M^{-1})
1-HSA	0.99×10^5	1.732×10^{13}	1.10	2.73×10^5
2-HSA	1.10×10^5	1.92×10^{13}	0.90	3.54×10^4

logarithmic plot (Figure 5 inset) thus obtained was used to estimate K_a, the equilibrium binding constant, and n, number of accessible binding sites for **1**–**2**, and these are presented in Table 2.

$$\log \frac{(F_0 - F)}{F} = \log K_a + n \log[Q] \quad (3)$$

The high K_a value suggests the complex's high affinity for HSA, and the value of n being close to 1 (Table 2) means that there is only one accessible binding site for the interaction of Cu(II) complexes **1**–**2** with HSA.

3.10.2. Synchronous Fluorescence. In HSA, chromophore Trp and Tyr residues are primarily responsible for its intrinsic fluorescence. Synchronous fluorescence spectroscopy is a common technique often used to assess conformational changes in HSA caused in the presence of a guest molecule.[66,67] Synchronous fluorescence spectrum is monitored by scanning simultaneously both excitation and emission wavelengths. When the $\Delta\lambda$ ($\Delta\lambda = \lambda_{em} - \lambda_{ex}$) values are maintained at 15 and 60 nm, synchronous fluorescence gives valuable information on the molecular microenvironment in the vicinity of Tyr and Trp residues of HSA, respectively.[72] A shift of emission maxima is directly related to the changes in polarity of chromospheres caused by addition of the guest molecule. If a blue shift is observed for λ_{max}, it means an increase in the hydrophobicity of the surrounding environment, while a red shift means increasing polarity of the surrounding environment as well as more exposure to solvent during the binding process.[66,67] In order to investigate the structural changes that occurred in HSA on binding of complexes **1**–**2**, varying concentrations of complexes were added, and synchronous fluorescence spectra were recorded. As can be seen in Figure 6A, at $\Delta\lambda$ = 15 nm with increasing concentration of complex **1**, the fluorescence intensity decreased by 30% from 3686 to 2597 au (λ_{max} = 300 nm). At $\Delta\lambda$ = 60 nm, considerable quenching of fluorescence intensity (by 40% from 8754 to 5270 au, λ_{max} = 340 nm) was noticed, but no shift in wavelength maxima occurred. The above observation indicates that the fluorescence intensity of both Tyr and Trp has been affected upon binding of **1** to HSA; however, the interaction between **1** and HSA alters conformation of Trp more than that in the Tyr microregion. The synchronous fluorescence spectra of HSA on addition of complex **2** (Figure 6B) resulted in quenching of fluorescence from 4879 to 2189 au, i.e., 55%, which is higher as compared to that for complex **1** at $\Delta\lambda$ = 15 nm and also a dramatic change from 10,000 to 2365 au, i.e., 76%, quenching was observed at $\Delta\lambda$ = 60 nm for **2**. The high decrease in fluorescence intensity indicates that **2** possibly binds in close proximity of Tyr and Trp. Also, when $\Delta\lambda$ = 15 nm, there is no shift, but when $\Delta\lambda$ = 60 nm, a red shift of 10 nm was observed (340 to 350 nm) with increasing concentration of complex **2** as can be seen in Figure 6B. These observations signify that the polarity around the Trp residue increases and hydrophobicity decreases on binding of **2** to HSA.

3.10.3. 3D Fluorescence Spectroscopy. 3D fluorescence spectroscopy enables easy visualization and provides detailed information regarding the conformational changes of protein upon ligand binding.[68] 3D spectra of HSA in the absence and presence of **1** and **2** are presented in Figures 7 and S18, respectively. Two peaks are found in the 3D spectra of HSA. Peak 1 represents the intrinsic fluorescence due to and Tyr and Trp residues, while peak 2 originates from the fluorescence of the polypeptide backbone and is associated with changes in HSA secondary structure.[68] It is observed from Figure 7 and Table 3 that an 18% drop in the fluorescence intensity of peak 1 and a drastic 64% drop in the intensity of peak 2 were resulted upon addition of complex **1** to HSA. Also, λ_{max} of HSA for peak 2 was blue-shifted by 4 nm in the presence of complex **1**; thus, we infer from these observations that binding of complex **1** to HSA led to conformational changes at the tertiary and secondary levels. The same experiment was conducted with complex **2** (Figure S18); the fluorescence intensity of peak 1 was seen to be diminished by 37% upon addition of complex **2** and was associated with 2 nm red shift, which indicates conformational changes resulting due to binding of **2** in proximity of Trp and Tyr amino acids. A drastic decrease (72%) in the intensity of peak 2 along with 10 nm blue shift was observed (Table S4), which indicates that **2** on binding also induces significant changes in the polypeptide backbone. Thus, it may be concluded that both complexes upon binding to HSA have altered the secondary and tertiary structures of HSA. Also, since a decrease in peak 2 is more

https://doi.org/10.1021/acsomega.3c01853
ACS Omega 2023, 8, 21948–21968

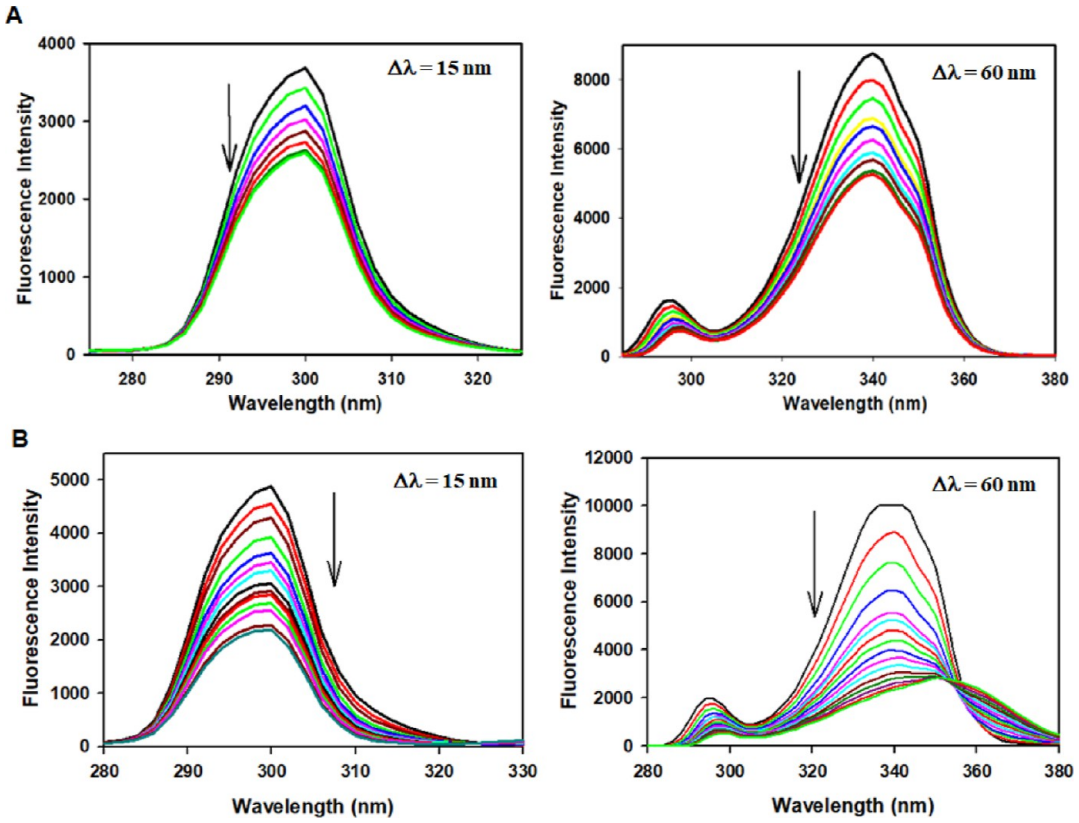

Figure 6. Synchronous quenching spectra of 4 μM HSA in 20 mM sodium phosphate buffer, pH 7.4, with (A) increasing concentration (0−8 μM) of **1** and (B) increasing concentration (0−15 μM) of **2** at $\Delta\lambda$ set as 15 nm and $\Delta\lambda$ set as 60 nm.

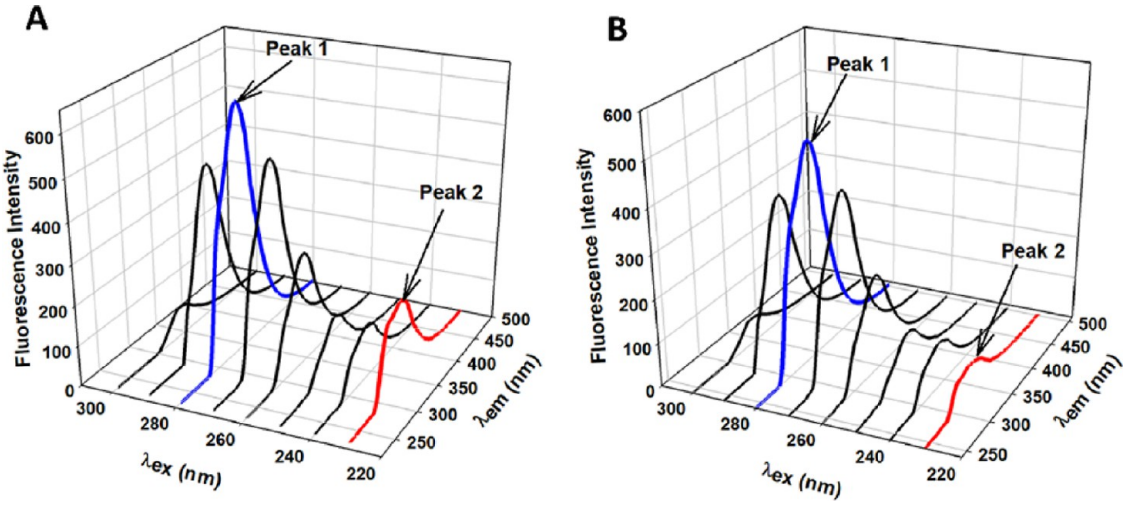

Figure 7. 3D fluorescence spectrum of (A) HSA (4 μM) and (B) HSA−complex **1** conjugate system having a concentration of 4 μM of each ([HSA]/[complex **1**] is 1:1).

Table 3. 3D Fluorescence Characteristic Parameters of HSA and HSA−Complex 1

	peak 1			peak 2		
	peak position ($\lambda_{ex}/\lambda_{em}$, nm/nm)	fluorescence intensity (au)	$\Delta\lambda$ (nm)	peak position ($\lambda_{ex}/\lambda_{em}$, nm/nm)	fluorescence intensity (au)	$\Delta\lambda$ (nm)
HSA	280/338	613.05	58	230/334	215.33	104
HSA + **1** (1:1)	280/338	497.60	58	230/330	77.40	100

than peak 1 for both complexes (**1**−**2**), it suggests that conformational changes in the polypeptide backbone is the dominant interaction.

3.10.4. Energy Transfer and Binding Distance. FRET occurs due to the interaction between the acceptor and the donor molecules in the excited state, resulting in energy transfer from

https://doi.org/10.1021/acsomega.3c01853
ACS Omega 2023, 8, 21948−21968

the donor to the acceptor when they are relatively close.[69,70] As can be seen in Figure 8, there is a significant overlap in the

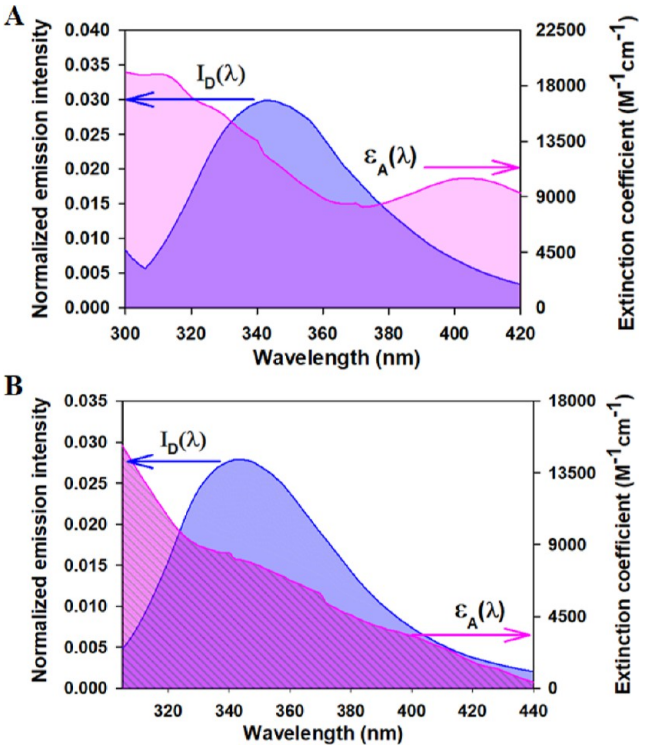

Figure 8. FRET: (A) overlap between the normalized emission spectrum of 4 μM HSA and the molar extinction coefficient spectrum of 4 μM complex **1**. (B) Overlap of the normalized emission spectrum of 4 μM HSA and the molar extinction coefficient spectrum of 4 μM of **2**.

emission spectra of the donor fluorophore (HSA) and the absorption spectrum of the acceptor (complexes **1** and **2** under study), and thus, efficient energy transfer is expected. FRET is generally employed as a guide to the localization of the binding site. The distance between the donor and the acceptor can be determined by FRET.[70]

E_{FRET} is the non-radiative energy transfer from the donor to the acceptor, and it is given by the relation

$$E_{FRET} = \frac{R_0^6}{R_0^6 + r^6} = 1 - \frac{F}{F_0} \quad (4)$$

In eq 4, r is the distance between donor and acceptor molecules and R_0 is the Förster radius, i.e., the distance between donor and acceptor such that E_{FRET} has the value of 0.5, while F_0 and F are the fluorescence emission intensities of the donor (HSA) in the absence and presence of the acceptor (complexes **1**−**2** under study). The Förster radius R_0 can be obtained using the following equation[69]

$$R_0 = 0.02108(K^2 \phi_D n^{-4} J)^{1/6} \quad (5)$$

The symbols used in eq 5 and their values assumed under the experimental conditions are as follows: K^2 is the spatial orientation factor and its value was considered as 2/3, ϕ_D is the fluorescence quantum yield of the donor and is taken as 0.118, n is the medium refractive index and taken as 1.33,[71] and J which is the degree of overlap is obtained from the relation[64]

$$J = \int \overline{I}_D(\lambda)\varepsilon_A(\lambda)\lambda^4 \, d\lambda \quad (6)$$

Once, the overlap integral J is determined, R_0 can be calculated using eq 5. Thus, Förster energy transfer parameters were calculated using eqs 4−6, and the calculated values of E_{FRET}, J, R_0, and r have been presented in Table 4. It is to be

Table 4. Förster Energy-Transfer Parameters of the Complex−HSA Interactions

complex	E_{FRET}	$J \times 10^{14}$ nm^4 M^{-1} cm^{-1}	R_0 nm	r nm
1-HSA	0.37	1.82	2.71	2.85
2-HSA	0.35	1.05	2.48	2.75

noted that the donor to acceptor distance should be between 2 and 8 nm[64] for occurrence of an efficient energy transfer. As can be seen from Table 4, the r values calculated for **1** and **2** are both in the expected 2−8 nm range and also obey the relation $0.5R_0 < r < 1.5R_0$, thus satisfying the conditions of Förster energy-transfer theory. The small values of r (Table 4) imply the high probability of energy transfer during the interaction between the complex (**1** or **2**) and HSA. These observations collectively suggest that both complexes **1**−**2** are in close proximity to HSA and explain the results of strong quenching of the intrinsic fluorescence of HSA in accordance with the static quenching mechanism involved in the interaction.

3.11. Molecular Docking with DNA. Molecular docking is a useful technique to study the drug−DNA interactions as the docking results provide information on position, affinity, and binding mode. In the present work, the interaction of Cu(II) complex **2** with B-DNA (PDB ID: 1BNA) was studied by molecular docking using AutoDock Vina to explore the precise binding site and find the aforementioned parameters. The best conformer pose of **2** with CT-DNA (Figure 9A) was selected for analysis, and the binding energy (ΔG) was found to be −7.1 kcal mol^{-1}. The more negative value of binding energy as compared to other reported Cu(II) Schiff base complexes[72] implies that complex **2** efficiently binds to DNA. Further, the binding energy was used to calculate the inhibitory constant using the relation $K_i = \exp(\Delta G/RT)$. Taking the value of R as 1.98×10^{-3} kcal mol^{-1} K^{-1} and temperature T as 298.15 K, the inhibition constant K_i was found to be 5.98 μM. Figure 9B shows the detailed illustration of binding interactions of complex **2** with DNA, and the molecule appears to intercalate between base pairs of CT-DNA. The docking results show that the imidazole co-ligand present in complex **2** formed two strong hydrogen bonds with DNA, one H-bond is between the imidazole N−H hydrogen atom and the oxygen atom of deoxy thymine (DTO2) with a bond length of 2.0 Å and the other H-bond is between the nitrogen atom of the deoxy adenine (DAN3) and the same imidazole hydrogen atom (N−H) of the co-ligand in complex **2** with a bond length of 2.9 Å. Also, a weak interaction (3.3 Å) can be seen between O2, the sulphinato oxygen (S−O$^-$) of the ligand with a sugar moiety. Thus, we may conclude that there is mutual agreement between DNA studies carried out by spectroscopic technique, viscosity measurements, and molecular docking results, and all of them support the intercalative mode of DNA binding.

3.12. Molecular Docking with HSA. It is a powerful technique used to identify the ligand binding sites in proteins. Docking studies using AutoDock Vina was done to find out the potential interaction site for **2** in HSA. It is known that HSA has three homologous domains, domain 1 comprises amino acid residues 1−197, domain II is composed of residues 198−382, and domain III has residues 383−585. There are two primary

https://doi.org/10.1021/acsomega.3c01853
ACS Omega 2023, 8, 21948−21968

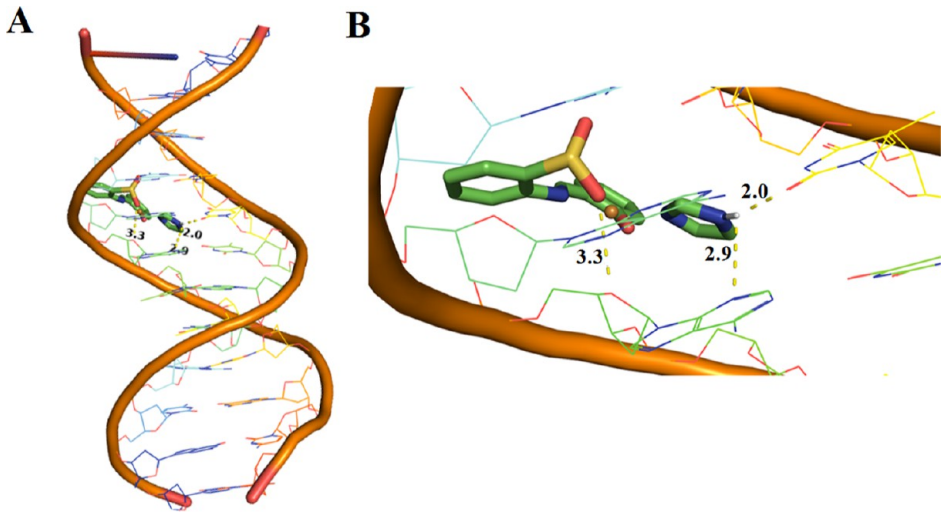

Figure 9. Molecular docking of complex **2** with CT-DNA. (A) Full view of docking pose of **2** in 1BNA. (B) Expanded view showing interactions between complex **2** and DNA by yellow dashed lines.

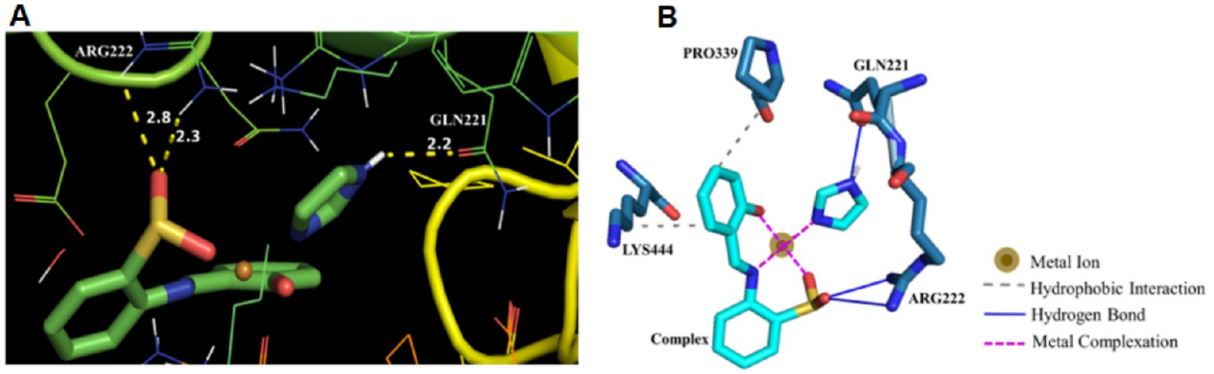

Figure 10. Interactions of complex **2** with HSA: (A) molecular docking showing the hydrogen bond interaction (yellow dashed line) between **2** and HSA. (B) Visualization of protein−ligand interaction generated by PLIP.

drug binding pockets, namely, Sudlow's site I in subdomain IIA and Sudlow's site II located in subdomain IIIA, also a third binding site is in subdomain IB named as site III. Also, Trp, the main fluorophore of HSA, is located in the large hydrophobic cavity in subdomain II (site I). The entrance of Sudlow's site I is surrounded by four basic amino acids, namely, Lys195, Lys199, Arg218, and Arg222.[16,64] Molecular docking of complex **2** with HSA done using AutoDock Vina is shown in Figure 10. For analysis, the best docking mode was selected, and the binding energy value obtained was −7.2 kcal/mol. As can be seen in Figure 10A, there was formation of two strong hydrogen bonds between 2HH1 and 2HH2 of Arg222 with O3 sulphinato (S═O) oxygen of the ligand with bond lengths 2.8 and 2.3 Å, respectively. Another strong H-bond interaction (2.2 Å) was noticed with OE1 of Gln221 and the N−H hydrogen atom of the imidazole co-ligand. The hydrogen bond interactions seen from docking studies (Figure 10A) clearly indicates that complex **2** primarily binds to site I of subdomain IIA of the HSA molecule. In extension, the protein−ligand interaction profiler (PLIP) was used for visualization and analysis of the docking results, and the detailed interactions resulting from binding of complex **2** with HSA are presented in Figure 10B and Table 5 showing labeled key residues present in the vicinity of the binding site. Three strong hydrogen bond interactions, of which one with Gln221 and two with Arg222, were observed; additionally, residues Pro339 and Lys444 were found to be involved in two mild hydrophobic interactions 3.92 and 3.45 Å (Figure 10B and Table 5). Therefore, from these observations, it can be concluded that the main interaction between complex **2** and HSA is in subdomain IIA. Also, it is to be noted that the interaction of **2** with amino acids Gln221 and Arg222 in particular are of specific importance as these residues are present at the entrance of the hydrophobic cavity of drug binding site I located in subdomain IIA where Trp 214 is also present; thus,

Table 5. Details of Molecular Interactions between HSA and 2 Using PLIP

	index	residue	distance (Å)	complex atom[a]	residue atom[a,b]
hydrogen bond interaction	1	Gln221	2.19	H3A	OE1
	2	Arg222	2.33	O3	2HH2
	3	Arg222	2.76	O3	2HH1
hydrophobic interaction	1	Pro339	3.92	C11	CB
	2	Lys444	3.45	C9	CD

[a]The first two characters of the atom name comprises chemical symbols used for specifying the atom type. Carbon atoms are specified by the letter "C"; nitrogen atoms are specified by the letter "N"; and oxygen atoms are specified by the letter "O". [b]In the case of amino acids, the next character stands for the remoteness indicator code, such as "B" used for β, "D" used for δ, and E used for ε.

https://doi.org/10.1021/acsomega.3c01853
ACS Omega 2023, 8, 21948−21968

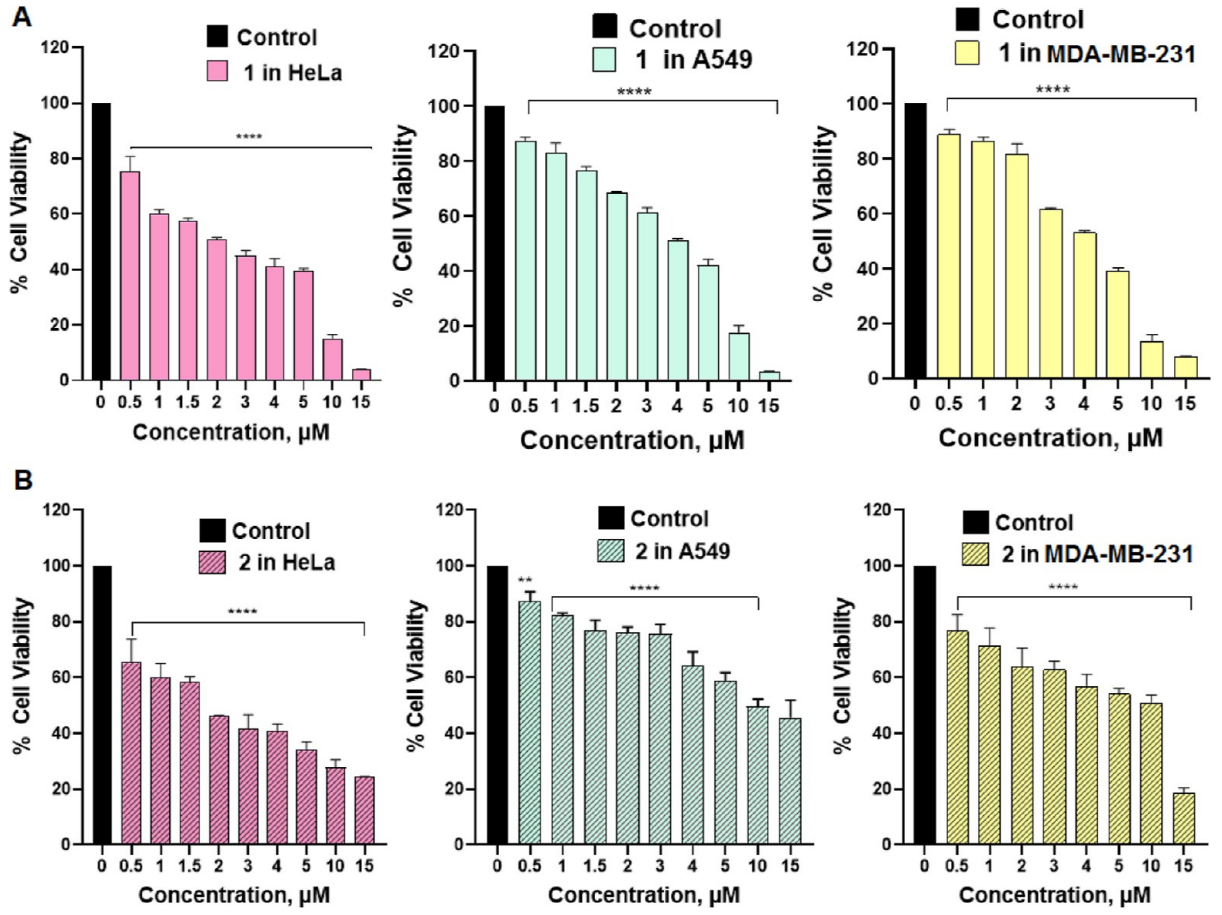

Figure 11. Cell viability of HeLa, A549, and MDA-MB-231 (A) treated with indicated concentrations of **1** and (B) treated with indicated concentrations of **2** and incubated for 24 h. Statistical analyses were done using graph pad prism. **** indicates $p < 0.0001$.

this fact further confirms that **2** binds in close proximity to tryptophan, which explains the drastic fluorescence quenching of tryptophan seen in the fluorescence-related studies.

3.13. Cytotoxicity Studies. *3.13.1. Inhibition of Cancer Cell Viability.* MTT (**1**−**2**, 3-(4,5-dimethylthiazol-2-yl)-2,5-diphenyltetrazolium bromide) is a commonly used colorimetric assay for determining cell metabolic activity. When MTT enters a cell, the mitochondrial activity of the cell reduces MTT to insoluble formazan, and the total mitochondrial activity is related to the number of viable cells.[73,74] From the plot of cell viability versus drug concentration, the half-maximal inhibitory concentration IC_{50} is determined, which is a measure of drug potency. In order to evaluate the cytotoxic potential of complexes **1**−**2**, the MTT assay was performed on three cancer cell lines, namely, cervical cancer HeLa, lung cancer A549, and breast cancer MDA-MB-231. Figure 11 depicts the cell viability with increasing complex concentration. It is to be noted that there is a sharp drop in cell viability for all the three cells tested at 10 μM dose of **1** (Figure 11A). In the case of **2**, both HeLa and A549 cells also showed a consistent decline in cell viability (Figure 11B). The calculated IC_{50} values for all the three cell lines with complexes **1**−**2** are summarized in Table 6 from which we can infer that complex **1** has IC_{50} values less than 5 μM in all the three cell lines. However, complex **2** shows maximum toxicity toward HeLa as evident from its IC_{50} value (1.86 ± 0.05) μM. Since both complexes **1**−**2** exhibit high cytotoxic potential in the HeLa cell line, further experiments were carried out on the HeLa cell line. As cisplatin is a commonly used drug for

Table 6. IC_{50} Values for the Compounds 1 and 2

cell line	IC_{50} (μM)	
	complex 1	complex 2
HeLa	2.04 ± 0.04	1.86 ± 0.05
A549	4.02 ± 0.07	12.97 ± 0.95
MDA-MB-231	4.16 ± 0.11	9.97 ± 0.03

successful treatment of most cancers, we performed the MTT assay using cisplatin on HeLa and MDA-MB-231 under similar experimental conditions (Figure S19). The IC_{50} value for cisplatin in HeLa was calculated as 30.93 ± 0.45 μM, while the breast cancer cells, i.e., MDA-MB-231, appeared to be resistant toward cisplatin as can be seen in Figure S19. Thus, in comparison to cisplatin, both complexes **1**−**2** in the present study show a significantly more cytotoxic behavior.

3.13.2. Nuclear Staining Assay. To find out the mechanism of cell death as well as to observe salient changes within the cells, various staining methods are used. Staining cells with Hoechst 33342 or AO/PI dual staining are ideal assays for distinguishing apoptotic cells from the healthy ones. Apoptosis leads to some distinct morphological changes in cells like shrinkage of cells, fragmentation of DNA, condensation of chromatin, and formation of apoptotic bodies.[75] The most characteristic feature of apoptosis is pyknosis, which is the result of chromatin condensation.[76] Representative pictures showing these morphological changes in HeLa cells treated with **1** undergoing apoptosis visualized by staining with Hoechst 33342 using

https://doi.org/10.1021/acsomega.3c01853
ACS Omega 2023, 8, 21948−21968

fluorescence microscopy are presented in Figure 12, and for **2**, these morphological changes are shown in Figure S20.

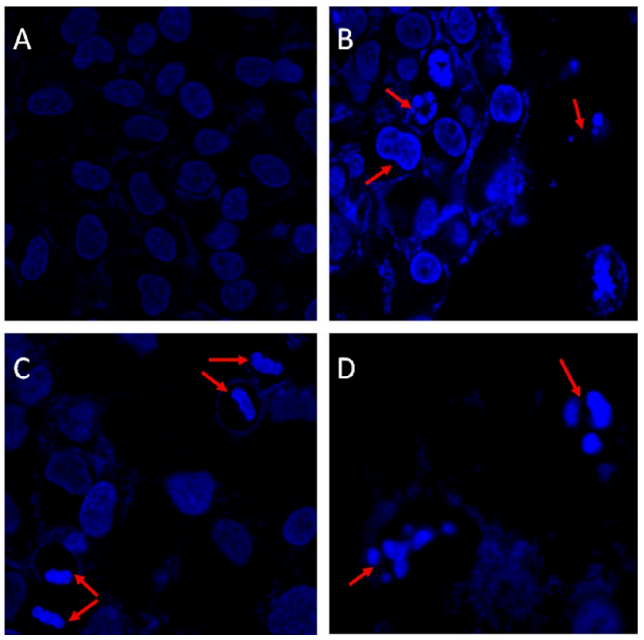

Figure 12. Apoptotic morphological changes in the nuclei of HeLa cells stained using Hoechst 33342 exposed to **1** for 24 h. (A) Untreated cells as a control and (B−D) treated cells with **1** showing chromatin condensation, cytoplasmic blebbing, and apoptotic bodies.

The results of increasing concentration of **1** and **2** on HeLa cells stained with Hoechst-33342 are presented in Figure 13. As can be seen, the control cells were homogeneous, uniformly presented blue staining, and showed no signs of fragmentation or condensation, while cells treated with IC_{50} dose (~2 μM) show clear signs of chromatin condensation. Half-moon (crescent)-shaped brightly stained apoptotic nuclei were visible. As we move on to 3 μM dose, there is significant loss in cell number as well as more fragmentation; condensation as well as shrinkage in the size of nucleus is observed. These results clearly indicate that **1** and **2** induced apoptosis in HeLa cells.

AO/PI dual staining was also used to observe the effects of **1**−**2** on HeLa cells. AO and PI are both nucleic acid binding dyes. AO penetrates into living cells, emitting green fluorescence, but it cannot differentiate between viable and non-viable cells. PI is able to permeate the altered cell membranes; it binds with the DNA of late apoptotic as well as secondary necrotic cells resulting orange fluorescence.[77−79] As observed from Figure 14, the control cells show green nuclei with no signs of fragmentation. Cells treated with 1 μM of each of complexes **1** and **2** have undergone morphological changes, and some of them emit green to slight orange fluorescence. These cells represent early apoptotic phase, while cells treated with the IC_{50} dose are less in number with respect to control and show cells from both early apoptotic phase (green-orange fluorescence) and late apoptotic phase (red-orange fluorescence).[77,78,80−82] At 3 μM concentration, a further reduction in cell number, along with shrunken and rounded nuclei, is seen. Also, more of them appear reddish-orange as they take up more PI due to severe nuclear damage, pointing that these cells have possibly reached the late apoptotic stage.

3.13.3. Caspase-3 Activity Assay. Caspases are crucial mediators of apoptosis. Most apoptotic programs follow either intrinsic or extrinsic pathway. Caspase-8 activation leads to an extrinsic pathway; on the other hand, caspase-9 activation leads to an intrinsic pathway, ultimately resulting in caspase-3 (following any of these pathways), one of the most important executioner caspase.[83] Caspase-3 plays a key role in nuclear apoptosis including chromatin condensation, DNA fragmentation, and cell blebbing. Thus, assays that can measure caspase-3 activity can be used to evaluate apoptosis-inducing agents. Caspase-3 activity can be easily monitored with the help of peptidic chromogenic or fluorogenic substrates with a specific peptidic sequence. Thus, in order to confirm that complexes **1**−**2** under study induces apoptosis, we analyzed the caspase activation (specifically caspase-3) in complex-treated HeLa cells using the caspase-3 colorimetric assay kit ab39401. This assay employs the synthetic tetrapeptide, Asp-Glu-Val-Asp (DEVD), labeled with *p*-nitroaniline (*p*-NA), a colorimetric molecule as a substrate. Caspase-3 catalyzes the hydrolysis of DEVD-*p*NA, subsequently releasing the chromophore *p*NA which has an absorption peak at 405 nm. This assay is based on

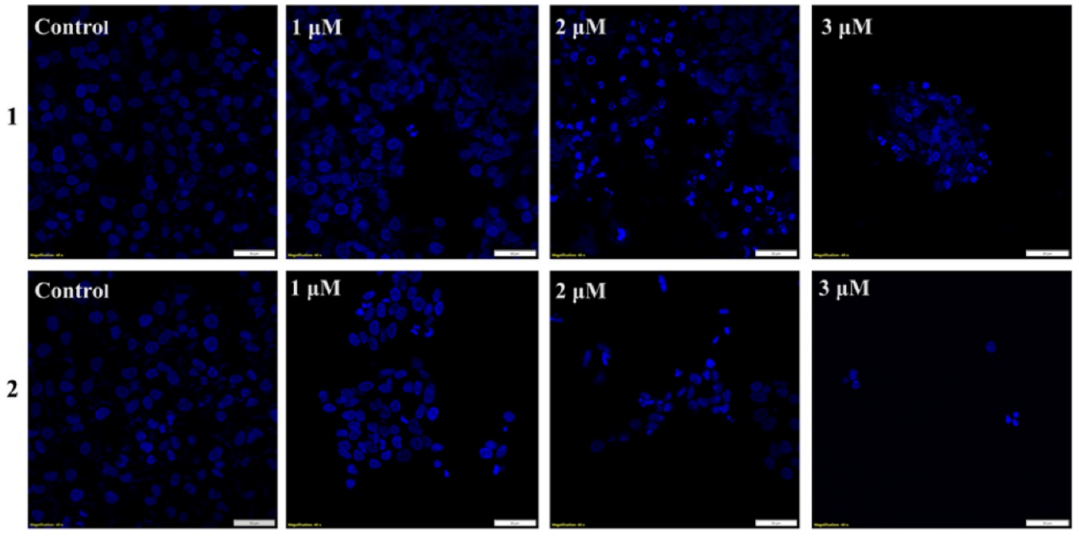

Figure 13. Hoechst-33342 staining of HeLa cells after 24 h exposure to compounds **1**−**2** with indicated concentrations. Scale bar: 50 μm.

https://doi.org/10.1021/acsomega.3c01853
ACS Omega 2023, 8, 21948−21968

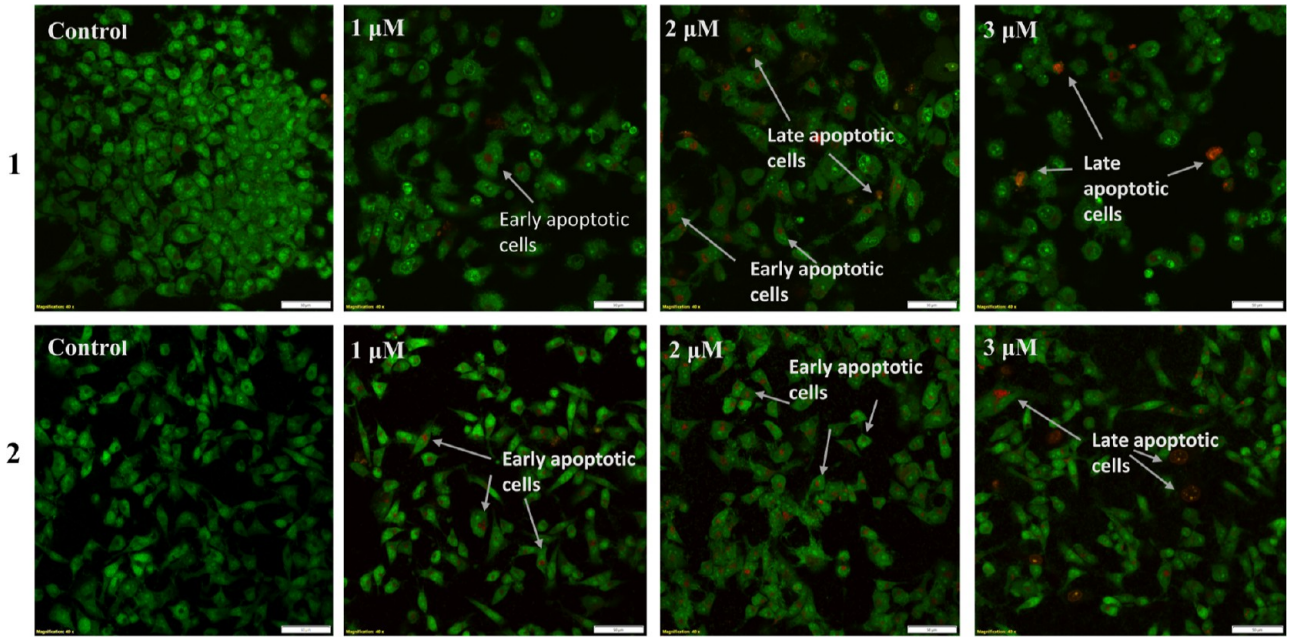

Figure 14. AO/PI staining of HeLa cells after treatment with **1** and **2** with concentrations as indicated for 24 h. Scale bar: 50 μm.

Scheme 2. Hydrolysis of DEVD-*p*NA to DEVD-OH and *p*NA as Catalyzed by Caspase-3

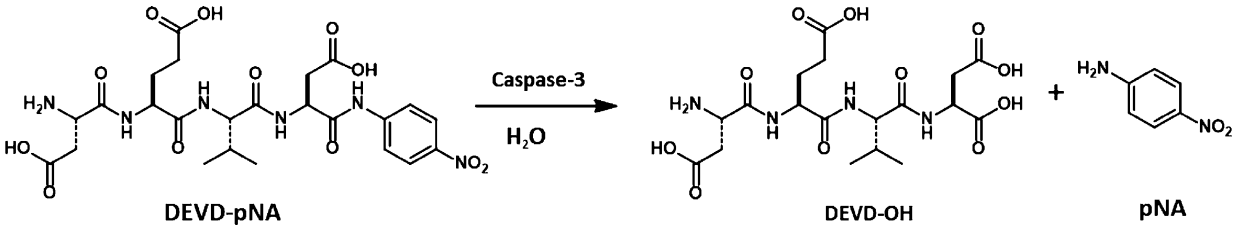

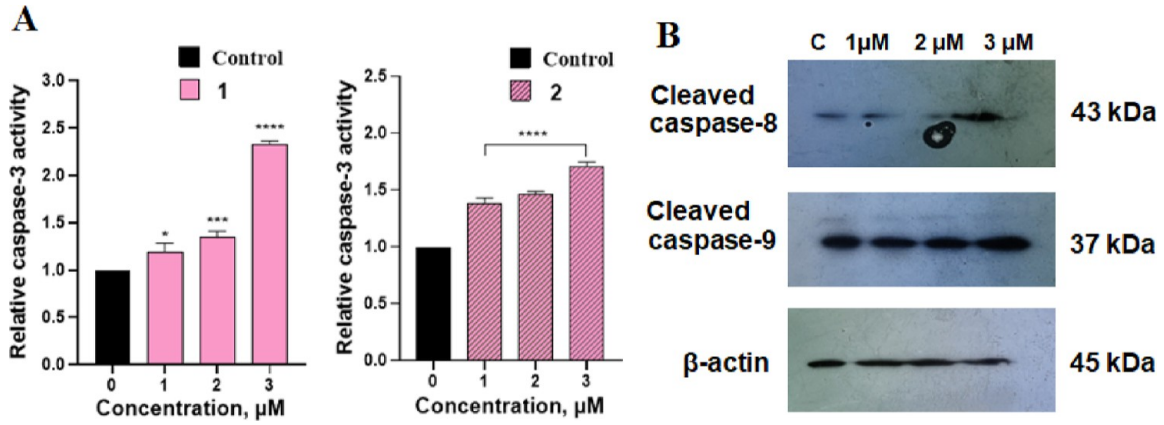

Figure 15. (A) Caspase-3 activity determined using colorimetric assay kit (ab39401) of HeLa cells treated with **1** and **2**. The absorbance intensity of treated samples was compared to that of untreated control to estimate the fold increase in caspase activity. The mean of three independent experiments conducted were considered. (B) Western blot analysis of complex **2**-treated HeLa cells showing the expression of cleaved caspase-9 and cleaved caspase-8 while β-actin was used as a loading control.

spectrophotometric detection of the chromophore *p*-nitroaniline resulting from the cleavage of the labeled substrate DEVD-*p*NA as shown in Scheme 2. Comparison of absorbance due to *p*-NA from the treated sample with that from untreated control allows us to assess the fold increase in caspase-3 activity.

The results of colorimetric assay performed to examine the role of complexes **1** and **2** in caspase-3 activation are demonstrated in Figure 15A. It can be seen that at 2 μM dose (close to IC_{50} value), compound **1** showed 1.3-fold and compound **2** showed almost 1.5-fold increase in caspase-3 activation in comparison to control comprising untreated cells. The caspase-3 activity further increased as the complex concentration is increased to 3 μM. Overall, these observations indicate that complexes **1**−**2** induced apoptosis in HeLa cells via caspase activation.

https://doi.org/10.1021/acsomega.3c01853
ACS Omega 2023, 8, 21948−21968

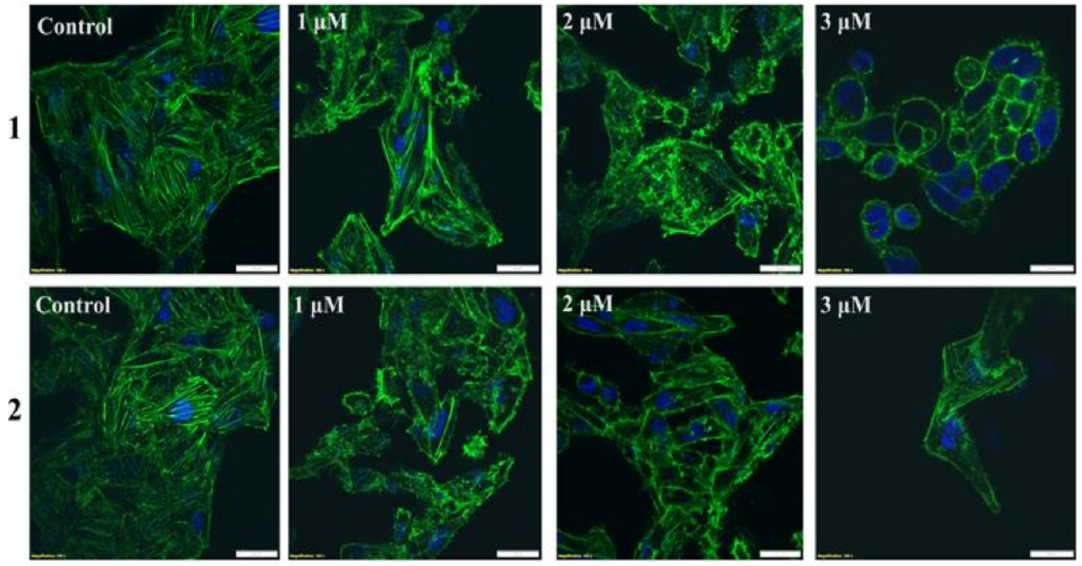

Figure 16. Confocal microscopy images of HeLa cells exposed to an increasing concentration of compounds **1**−**2** for 24 h and stained with Phalloidin and Hoechst-33342. Scale bar: 20 μm.

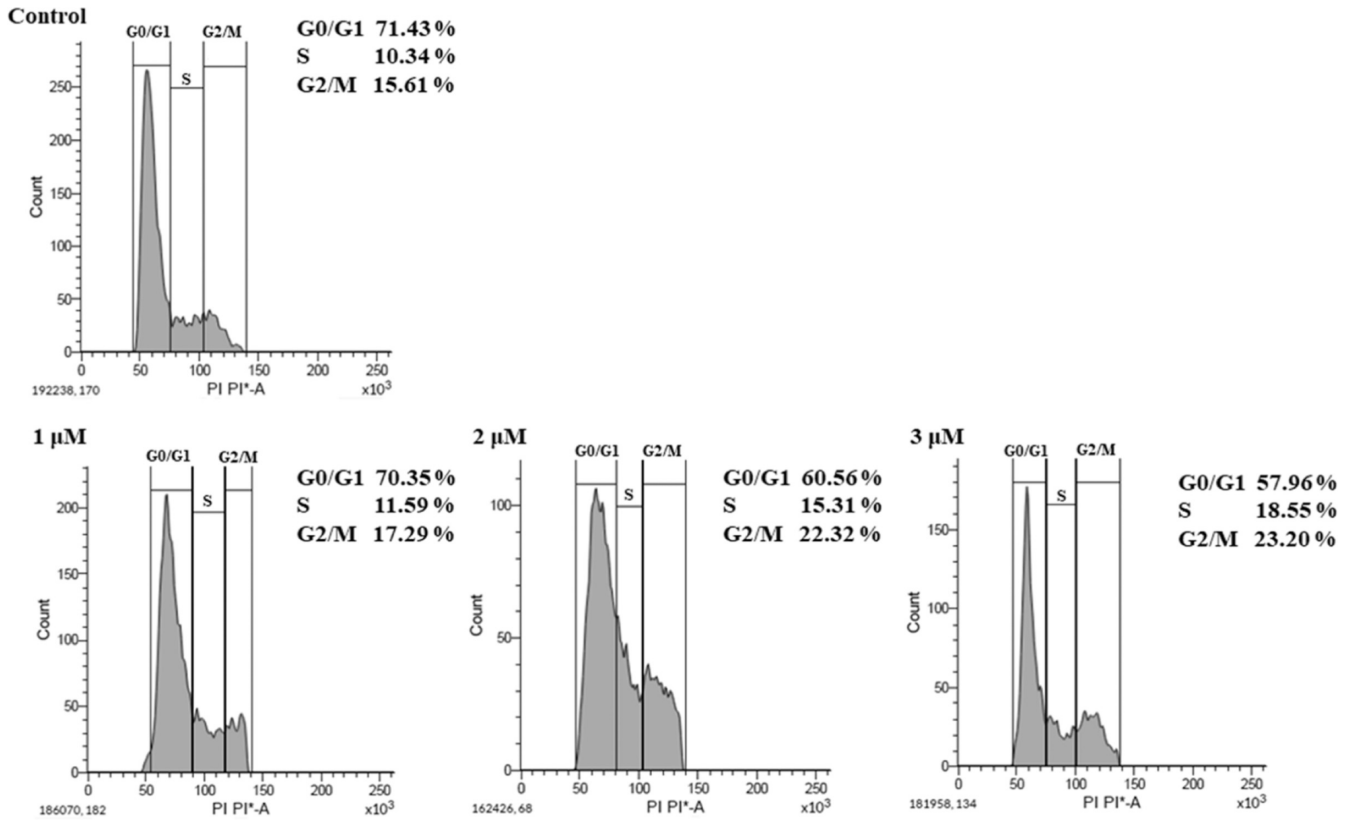

Figure 17. Cell population in percentage at different phases of cell cycle before and after treatment with indicated concentrations of complex **1**.

3.13.4. Western Blot Analysis. Once it was established that there was prominent caspase-3 activation by both complexes, our next aim was to identify the exact apoptotic pathway followed. Therefore, we performed western blot on complex **2**-treated HeLa cells with caspase 8 and caspase 9 to check if the pathway is extrinsic or intrinsic. As can be seen from Figure 15B, there is significant increase in cleaved caspase 9 expression, which follows a dose-dependent pattern, while the expression level for cleaved caspase 8 is not that significant. Loading control β-actin expression remains constant for all lanes. Thus, we may conclude that the apoptosis induced by the Cu(II) complex **2** under study is primarily mediated via the intrinsic pathway.

3.13.5. Actin Staining. During apoptosis, cells undergo various morphological changes where cytoskeleton participates actively. According to the literature, caspases upon activation cleave the cytoskeleton actin and accelerates the apoptotic process resulting in physical changes that are hallmarks of apoptosis.[84] Phalloidin is a highly selective bicyclic peptide used for staining actin filaments. Thus, to see the effects of **1**−**2** on the actin filaments, HeLa cells were stained with phalloidin-iFluor

https://doi.org/10.1021/acsomega.3c01853
ACS Omega 2023, 8, 21948−21968

488 and Hoechst 33342. Upon staining HeLa cells with Phalloidin, it was observed that both complexes cause significant damage to the actin filaments as compared to untreated control cells (Figure 16). Both control images show intact green filaments which represent a healthy actin cytoskeleton, while on treatment with the copper(II) complexes (**1**−**2**), there is clear damage of actin filaments. This damage to actin filaments increases for both complexes with increasing concentration while the cell population decreases. In complex **1**, the 1 μM concentration shows few intact actin filaments; upon further increasing complex **1** concentration, the cells at 3 μM dose look round with loss in actin density around the nucleus. Similar results are seen for complex **2** as well. However, for complex **2**, the damage to actin filaments is higher at 1 μM dose itself when compared to complex **1**. These results indicate that both complexes are causing destruction in actin filaments along with nuclear fragmentation which may lead to apoptosis.

3.13.6. Analysis of Cell Cycle Progression. All cancer cells show an abnormal property of unregulated cell division. They keep dividing bypassing cell cycle checkpoints and form tumor masses which invade neighboring cells and organs, ultimately spreading throughout the body.[74] To understand the effect of **1** and **2** on cell cycle progression, cell cycle analysis was done on PI-stained HeLa cells with the help of FACS. A representative figure of HeLa cells treated with different amounts (1, 2, and 3 μM) of **1** for 24 h showing a typical DNA pattern that represented G0/G1, S, and G2/M phases of the cell cycle is depicted in Figure 17. As can be seen, there is a significant decrease in the G0/G1 phase (71% in control to 58% at 3 μM) and a prominent increase in the S phase of the cell cycle, wherein the DNA gets replicated. There is 5% increase in the cell population in the S phase at the IC_{50} dose (~2 μM) and 8.2% increase in the S phase at 3 μM concentration as compared to control. Thus, an increase in cell population in the S-phase is in a dose-dependent manner. Also, cells which were able to cross the S phase are seen to be further arrested in the G2/M phase as the cell population is seen to steadily increase in this phase and reached 23% at 3 μM dose from 15.6% in control (Figure 17). The effect of complex **2** on cell cycle progression (Figure S21) shows a similar trend to complex **1**. The cell population decreased in the G0/G1 phase, and a steady increase in S phase and G2/M phase was observed when the treatment concentration of **2** was increased from 1 to 3 μM. Here also, HeLa cells that were able to pass through the S phase and replicate their DNA got arrested in the next phase, i.e., G2/M phase. This experiment suggests that complexes **1** and **2** induced arrest in both S and G2/M phases of the cell cycle, and uncontrolled progression of cancer cells can be inhibited to some extent upon treatment by complexes **1**−**2**.

4. CONCLUSIONS

In summary, a copper(II) thiolate complex **1** and its corresponding sulfinato-complex **2** containing the imidazole co-ligand have been prepared and characterized with the help of elemental analyses and HRMS, XPS, IR, UV−vis, and EPR spectroscopic as well as cyclic voltammetric studies. Complex **2** has also been characterized crystallographically; it has distorted square-pyramidal geometry with a central copper atom coordinated through the tridentate ligand and the imidazole moiety. Most importantly, **2** was found to be soluble and stable in water, and possibly, this is the first report of a water-soluble stable Cu^{II}−sulfinato complex produced by aerial oxidation of its thiolato complex **1**. The interaction of **1**−**2** with CT-DNA studied using absorption titration and viscosity measurements indicated the intercalative mode of binding to DNA. Both complexes displayed significant cleavage of pUC19 DNA in the presence of hydrogen peroxide. Additionally, complex **2** was also capable of promoting DNA cleavage in the absence of any external agent or light. The interaction between the complexes **1**−**2** and HSA was also investigated. Fluorescence quenching results indicated the static quenching mechanism upon binding of the complexes to HSA. Synchronous and 3D studies revealed that the complexes cause conformational changes in the microenvironment of tyrosine and tryptophan residues and the protein backbone on binding to HSA. From molecular docking, it can be concluded that complex **2** was bound to site I of HSA, which is located in the hydrophobic pocket of subdomain IIA. The complexes **1**−**2** showed strong in vitro antiproliferative activity against various cancer cells (HeLa, A549, and MDA-MB-231). Both **1**−**2** appear to be highly potent against cervical cancer HeLa cells as revealed from their low cell viability (IC_{50} values of 2.04 μM for **1** and 1.86 μM for **2**). Complex **1** is more sensitive to A549 than **2** (IC_{50} = 4.02 μM for **1** and 12.97 μM for **2**). Also, cisplatin-resistant MDA-MB-231 breast cancer cells displayed remarkable sensitivity to the tested compounds **1**−**2** (4.16 μM for **1** and 9.97 μM for **2**). Thus, complexes **1**−**2** act as potent antiproliferative agents by inducing morphological changes as can be seen from nuclear staining and caspase activation via the intrinsic mitochondrial pathway, leading to apoptotic cell death. Flow cytometric analysis showed that **1** as well as **2** inhibited the growth of HeLa cells through cell cycle arrest in both S phase and G2/M phase.

■ ASSOCIATED CONTENT

Supporting Information

The Supporting Information is available free of charge at https://pubs.acs.org/doi/10.1021/acsomega.3c01853.

Additional experimental details, materials, and physical measurements; ESI-MS, infrared, UV−vis, XPS, and EPR spectra; cyclic voltammograms; DNA binding; viscosity of CT-DNA; hydrolytic cleavage of pUC19 DNA; 3D fluorescence spectra of HSA; cell viability of HeLa and MDA-MB-231 cells; apoptotic morphological changes in HeLa cells; cell cycle analysis; and single-crystal X-ray diffraction data and 3D fluorescence spectral results (PDF)

CCDC 2246009 containing the supplementary crystallographic data for compound 2 can be obtained free of charge via http via www.ccdc.cam.ac.uk/data_request/cif, or by emailing data_request@ccdc.cam.ac.uk, or from the Cambridge Crystallographic Data Centre, 12 Union Road, Cambridge CB2 1EZ, UK; Fax: (+044) 1223-336-033 (CIF)

■ AUTHOR INFORMATION

Corresponding Author

Manjuri Kumar − *Department of Chemical Engineering, Birla Institute of Technology and Science-Pilani, Zuarinagar 403726 Goa, India;* orcid.org/0000-0002-8102-8923; Email: manjuri@goa.bits-pilani.ac.in

Authors

Kumudini Paliwal − *Department of Chemical Engineering, Birla Institute of Technology and Science-Pilani, Zuarinagar 403726 Goa, India;* orcid.org/0000-0002-6985-3381

Paramita Haldar − *Department of Chemical Engineering, Birla Institute of Technology and Science-Pilani, Zuarinagar 403726 Goa, India;* orcid.org/0000-0003-1614-3180

P. K. Sudhadevi Antharjanam − *Sophisticated Analytical Instrument Facility, Indian Institute of Technology-Madras, Chennai 600 036, India;* orcid.org/0000-0002-8801-7530

Complete contact information is available at: https://pubs.acs.org/10.1021/acsomega.3c01853

Notes

The authors declare no competing financial interest.

■ ACKNOWLEDGMENTS

We thank the SAIF, IIT-Madras, for XRD; SAIF, IIT-Bombay, for EPR; and the CSIR-National Chemical Laboratory (NCL), Pune, for XPS and HRMS facilities. M.K. thanks Dr. C.S. Gopinath, Chair, Catalysis and Inorganic Chemistry Division, NCL, Pune, for help with the XPS and HRMS studies. M.K. also thanks Prof. P.B., Department of Chemistry, BITS Pilani, K. K. Birla Goa Campus for help with the cyclic voltammetric studies, and Prof. R.D., Head, Department of Chemistry, NIT Rourkela, for help with ESI-MS for compound **2**. We gratefully acknowledge the Department of Biological Sciences, BITS Pilani, K. K. Birla Goa Campus, for providing us the cell culture facility and cell cycle analysis. We also thank the CSIF, BITS Pilani, K. K. Birla Goa Campus, for providing instrumental facility.

■ REFERENCES

(1) Santini, C.; Pellei, M.; Gandin, V.; Porchia, M.; Tisato, F.; Marzano, C. Advances in Copper Complexes as Anticancer Agents. *Chem. Rev.* **2014**, *114*, 815−862.

(2) Barone, G.; Terenzi, A.; Lauria, A.; Almerico, A. M.; Leal, J. M.; Busto, N.; García, B. DNA-binding of Nickel(II), Copper(II) and Zinc(II) Complexes: Structure−affinity Relationships. *Coord. Chem. Rev.* **2013**, *257*, 2848−2862.

(3) Allen, S. E.; Walvoord, R. R.; Padilla-Salinas, R.; Kozlowski, M. C. Aerobic Copper-Catalyzed Organic Reactions. *Chem. Rev.* **2013**, *113*, 6234−6458.

(4) Jang, H.-Y. Oxidative Cross-coupling of Thiols for S−X (X = S, N, O, P, and C) Bond Formation: Mechanistic Aspects. *Org. Biomol. Chem.* **2021**, *19*, 8656−8686.

(5) Ohui, K.; Afanasenko, E.; Bacher, F.; Ting, R. L. X.; Zafar, A.; Blanco-Cabra, N.; Torrents, E.; Dömötör, O.; May, N. V.; Darvasiova, D.; Enyedy, E. A.; Popović-Bijelić, A.; Reynisson, J.; Rapta, P.; Babak, M. V.; Pastorin, G.; Arion, V. B. New Water-Soluble Copper(II) Complexes with Morpholine−Thiosemicarbazone Hybrids: Insights into the Anticancer and Antibacterial Mode of Action. *J. Med. Chem.* **2019**, *62*, 512−530.

(6) Sorenson, J. R. J. Copper Chelates as Possible Active Forms of the Antiarthritic Agents. *J. Med. Chem.* **1976**, *19*, 135−148.

(7) Szymański, P.; Frączek, T.; Markowicz, M.; Mikiciuk-Olasik, E. Development of Copper Based Drugs, Radiopharmaceuticals and Medical Materials. *BioMetals* **2012**, *25*, 1089−1112.

(8) da Silva, D. A.; De Luca, A.; Squitti, R.; Rongioletti, M.; Rossi, L.; Machado, C. M. L.; Cerchiaro, G. Copper in Tumors and the Use of Copper-based Compounds in Cancer Treatment. *J. Inorg. Biochem.* **2022**, *226*, 111634.

(9) Smith, R. C.; Reed, V. D.; Hill, W. E. Oxidation of Thiols by Copper(II). *Phosphorus, Sulfur Silicon Relat. Elem.* **1994**, *90*, 147−154.

(10) Feldman, S. L.; Hunter, J. S. V.; Zgirski, A.; Chidambaram, M. V.; Frieden, E. Comparison of the Catalytic Oxidation of Cysteine and *o*-Dianisidine by Cupric Ion and Ceruloplasmin. *J. Inorg. Biochem.* **1982**, *17*, 51−60.

(11) Farid Khan, M.; Sorenson, J. R. J. Copper(II) (3,5-diisopropylsalicylate)$_2$ Oxidizes Thiols to Symmetrical Disulfides and Oxidatively Converts Mixtures of 5-Thio-2-nitrobenzoic Acid and Nonsymmetrical 5-Thio-2-nitrobenzoic Acid Disulfides to Symmetrical Disulfides. *J. Inorg. Biochem.* **1991**, *41*, 221−234.

(12) Freedman, J. H.; Ciriolo, M. R.; Peisach, J. The Role of Glutathione in Copper Metabolism and Toxicity. *J. Biol. Chem.* **1989**, *264*, 5598−5605.

(13) Ciriolo, M. R.; Desideri, A.; Paci, M.; Rotilio, G. Reconstitution of Cu,Zn-Superoxide Dismutase by the Cu(I) Glutathione Complex. *J. Biol. Chem.* **1990**, *265*, 11030−11034.

(14) Patel, R. N.; Gundla, V. L. N.; Patel, D. K. Synthesis Characterization and Properties of Some Ternary Copper(II) Complexes Containing NOS Donor Schiff Base and NN Donor Bidentate Ligands. *Indian J. Chem.* **2008**, *47A*, 353−360.

(15) Kumar, M.; Parsekar, S. U.; Duraipandy, N.; Kiran, M. S.; Koley, A. P. S. DNA Binding and in vitro Cytotoxicity Studies of a Mononuclear Copper(II) Complex Containing N_2S(thiolate)Cu Core and 1,10-Phenanthroline as a Coligand. *Inorg. Chim. Acta* **2019**, *484*, 219−226.

(16) Paliwal, K.; Haldar, P.; Antharjanam, P. K. S.; Kumar, M. Mixed Ligand Mononuclear Copper(II) Complex as a Promising Anticancer Agent: Interaction Studies with DNA/HSA, Molecular Docking, and *in vitro* Cytotoxicity Studies. *ACS Omega* **2022**, *7*, 21961−21977.

(17) Bolos, C. A.; Chaviara, A. T.; Mourelatos, D.; Iakovidou, Z.; Mioglou, E.; Chrysogelou, E.; Papageorgiou, A. Synthesis, Characterization, Toxicity, Cytogenetic and in vivo Antitumor Studies of 1,1-Dithiolate Cu(II) Complexes with di-tri-tetra- amines and 1,3-thiazoles. Structure-activity Correlation. *Bioorg. Med. Chem.* **2009**, *17*, 3142−3151.

(18) Raman, N.; Jeyamurugan, R.; Senthilkumar, R.; Rajkapoor, B.; Franzblau, S. G. In vivo and in vitro Evaluation of Highly Specific Thiolate Carrier Group Copper(II) and Zinc(II) Complexes on Ehrlich Ascites Carcinoma Tumor Model. *Eur. J. Med. Chem.* **2010**, *45*, 5438−5451.

(19) Higashi, L. S.; Lundeen, M.; Hilti, E.; Seff, K. Crystal and Molecular Structure of Bis(2-pyridine sulfinato)copper(II). *Inorg. Chem.* **1977**, *16*, 310−313.

(20) Langs, D. A.; Hare, C. R. The Structure of Bis-(toluene-*p*-sulphinato)copper(II) tetrahydrate. *Chem. Commun.* **1967**, 853−854.

(21) Qi, J.; Zhang, Y.; Gou, Y.; Zhang, Z.; Zhou, Z.; Wu, X.; Yang, F.; Liang, H. Developing an Anticancer Copper(II) Pro-drug Based on the His242 Residue of the Human Serum Albumin Carrier IIA Subdomain. *Mol. Pharm.* **2016**, *13*, 1501−1507.

(22) Shen, F.; Liu, Y. X.; Li, S. M.; Jiang, C. K.; Wang, B. F.; Xiong, Y. H.; Mao, Z. W.; Le, X. Y. Synthesis, Crystal Structures, Molecular Docking and in vitro Cytotoxicity Studies of Two New Copper(II) Complexes: Special Emphasis on Their Binding to HSA. *New J. Chem.* **2017**, *41*, 12429−12441.

(23) Koley, M.; Sivasubramanian, S. C.; Varghese, B.; Manoharan, P. T.; Koley, A. P. Synthesis and Characterization of Two Stable Paramagnetic Octahedral Chromium(IV) Complexes with Dianionic Tridentate SNO Donor Ligands and of a Chromium(III) Complex with a ONO Donor Ligand. *Inorg. Chim. Acta* **2008**, *361*, 1485−1495.

(24) Fandos, R.; Otero, A.; Rodríguez, A. M.; Suizo, S. Monocyclopentadienyl Titanium Complexes Supported by Functionalized Shiff Base Ligands. *J. Organomet. Chem.* **2014**, *759*, 74−82.

(25) Bruker. *Apex3 v2017.3-0, SAINT V8.38A*; Bruker AXS Inc: Madison (WI), USA, 2016.

(26) Sheldrick, G. M. SHELXT−Integrated Space-Group and Crystal structure Determination. *Acta Crystallogr., Sect. A: Found. Adv.* **2015**, *71*, 3−8.

(27) Sheldrick, G. M. Crystal Structure Refinement with SHELXL. *Acta Crystallogr., Sect. C: Struct. Chem.* **2015**, *71*, 3−8.

(28) Farrugia, L. J. WinGX and ORTEP for Windows: An Update. *J. Appl. Crystallogr.* **2012**, *45*, 849−854.

(29) Parsekar, S. U.; Haldar, P.; Sudhadevi Antharjanam, P. K.; Kumar, M.; Koley, A. P. Synthesis, Characterization, Crystal Structure, DNA and Human Serum Albumin Interactions, as well as

Antiproliferative Activity of a Cu(II) Complex Containing a Schiff Base Ligand Formed in situ from the Cu(II)-induced Cyclization of 1,5-Bis(salicylidene)thiocarbohydrazide. *Appl. Organomet. Chem.* **2021**, *35*, No. e6152.

(30) Berendsen, H. J. C.; Van der Spoel, D.; van Drunen, R. GROMACS: A message-passing parallel molecular dynamics implementation. *Comput. Phys. Commun.* **1995**, *91*, 43−56.

(31) Trott, O.; Olson, A. J. AutoDock Vina: Improving the Speed and Accuracy of Docking With a New Scoring Function, Efficient Optimization, and Multithreading. *J. Comput. Chem.* **2010**, *31*, 455−461.

(32) Eberhardt, J.; Santos-Martins, D.; Tillack, A. F.; Forli, S. AutoDock Vina 1.2.0: New Docking Methods, Expanded Force Field, and Python Bindings. *J. Chem. Inf. Model.* **2021**, *61*, 3891−3898.

(33) Lindahl, E.; Hess, B.; van der Spoel, D. GROMACS 3.0: A Package for Molecular Simulation and Trajectory Analysis. *J. Mol. Model.* **2001**, *7*, 306−317.

(34) Allen, M. P.; Tildesley, D. J. *Computer Simulation of Liquids*; Clarendon Press, 1987.

(35) Adasme, M. F.; Linnemann, K. L.; Bolz, S. N.; Kaiser, F.; Salentin, S.; Haupt, V. J.; Schroeder, M. PLIP 2021: Expanding the Scope of the Protein−Ligand Interaction Profiler to DNA and RNA. *Nucleic Acids Res.* **2021**, *49*, W530−W534.

(36) Moosun, S. B.; Jhaumeer-Laulloo, S.; Hosten, E. C.; Gerber, T. I. A.; Bhowon, M. G. Antioxidant and DNA Binding Studies of Cu(II) Complexes of N,N′-(1,1′-dithio-bis(phenylene))-bis-(salicylideneimine): Synthesis and Characterization. *Transition Met. Chem.* **2015**, *40*, 445−458.

(37) Wu, Y.-R.; Chang, C.-M.; Wang, C.-C.; Hsieh, C.-C.; Horng, Y.-C. C=N Bond Activation and Hydration by an Iron(III) Complex with Asymmetric Sulfur Oxygenation. *Eur. J. Inorg. Chem.* **2017**, *2017*, 840−843.

(38) Cavell, A. C.; Hartley, C. L.; Liu, D.; Tribble, C. S.; McNamara, W. R. Sulfinato Iron(III) Complex for Electrocatalytic Proton Reduction. *Inorg. Chem.* **2015**, *54*, 3325−3330.

(39) Noveron, J. C.; Olmstead, M. M.; Mascharak, P. K. A Synthetic Analogue of the Active Site of Fe-Containing Nitrile Hydratase with Carboxamido N and Thiolato S as Donors: Synthesis, Structure, and Reactivities. *J. Am. Chem. Soc.* **2001**, *123*, 3247−3259.

(40) Kumar, M.; Colpas, G. J.; Day, R. O.; Maroney, M. J. Ligand Oxidation in a Nickel Thiolate Complex: A Model for the Deactivation of Hydrogenase by Oxygen. *J. Am. Chem. Soc.* **1989**, *111*, 8323−8325.

(41) Mirza, S. A.; Pressler, M. A.; Kumar, M.; Day, R. O.; Maroney, M. J. Oxidation of Nickel Thiolate Ligands by Dioxygen. *Inorg. Chem.* **1993**, *32*, 977−987.

(42) Nicholson, T.; Zubieta, J. Coordination Chemistry of the Rhenium-organodiazenido Core with Facultative Tetradentate Ligands Possessing Thiolate-amine and Thiolate-thioether Donor Sets. Crystal and Molecular Structures of [Re-($SCH_2CH_2NMeCH_2CH_2NMeCH_2CH_2S$)($N_2COC_6H_4$-*p*-Cl)-($PPh_3$)].$CH_3OH$, [Re($SCH_2CH_2S(CH_2)_3SCH_2CH_2S$)($N_2COPh$)-($PPh_3$)], and [Re($SCH_2CH_2S(CH_2)_3SCH_2CH_2S$)($N_2CO_2Me$)-($PPh_3$)].$CH_2Cl_2$ and a Comparison with the Structure of the Oxidation Product [N,N'-dimethyl-N,N'-bis(sulfinatoethyl)-ethylenediamine-S,N,N',O'] [(2-chlorophenyl)diazenido]-(triphenylphosphine)rhenium (I), [Re-($O_2SCH_2CH_2NMeCH_2CH_2NMeCH_2CH_2S$ O_2)($N_2C_6H_4$-*o*-Cl)-(PPh3)]. *Inorg. Chem.* **1987**, *26*, 2094−2101.

(43) Naik, B.; Parida, K. M.; Gopinath, C. S. Facile Synthesis of N- and S-Incorporated Nanocrystalline TiO_2 and Direct Solar-Light-Driven Photocatalytic Activity. *J. Phys. Chem. C* **2010**, *114*, 19473−19482.

(44) Smart, R. S. C.; Skinner, W. M.; Gerson, A. R. XPS of Sulphide Mineral Surfaces: Metal-deficient, Polysulphides, Defects and Elemental Sulphur. *Surf. Interface Anal.* **1999**, *28*, 101−105.

(45) Koley, A. P.; Nirmala, R.; Prasad, L. S.; Ghosh, S.; Manoharan, P. T. Studies on Gold(I1) Complexes with Hard and Soft Donor Ligands. 3. Complexes with *N*- (2-Pyridylmethyl)-2-mercaptoaniline. *Inorg. Chem.* **1992**, *31*, 1764−1769.

(46) Naumkin, A. V.; Kraut-Vass, A.; Gaarenstroom, S. W.; Powell, C. J. *NIST X-ray Photoelectron Spectroscopy Database: NIST Standard Reference Database 20*, Version 4.1, 2012.

(47) Addison, A. W.; Rao, T. N.; Reedijk, J.; van Rijn, J.; Verschoor, G. C. Synthesis, Structure, and Spectroscopic Properties of Copper(II) Compounds Containing Nitrogen−Sulphur Donor Ligands; the Crystal and Molecular Structure of Aqua[1,7-bis(N-methylbenzimidazol-2′-yl)-2,6-dithiaheptane]copper(II) perchlorate. *J. Chem. Soc., Dalton Trans.* **1984**, *7*, 1349−1356.

(48) Selvakumar, B.; Rajendiran, V.; Uma Maheswari, P.; Stoeckli-Evans, H.; Palaniandavar, M. Structures, Spectra, and DNA-binding Properties of Mixed Ligand Copper (II) Complexes of Iminodiacetic acid: The Novel Role of Diimine Co-ligands on DNA Conformation and Hydrolytic and Oxidative Double Strand DNA Cleavage. *J. Inorg. Biochem.* **2006**, *100*, 316−330.

(49) Rabindra Reddy, P.; Shilpa, A. Synthesis, Characterization, and DNA -Binding and Cleavage Properties of Dinuclear Cu^{II}-Salophen/Salen Complexes. *Chemistry & Biodiversity* **2011**, *8*, 1245−1265.

(50) Gao, E. J.; Wang, L.; Zhu, M. C.; Liu, L.; Zhang, W. Z. Synthesis, Characterization, Interaction with DNA and Cytotoxicity in vitro of the Complexes [M (dmphen)(CO_3)]·H_2O [M= Pt (II), Pd (II)]. *Eur. J. Med. Chem.* **2010**, *45*, 311−316.

(51) Wolfe, A.; Shimer, G. H., Jr.; Meehan, T. Polycyclic Aromatic Hydrocarbons Physically Intercalate into Duplex Regions of Denatured DNA. *Biochemistry* **1987**, *26*, 6392−6396.

(52) Strothkamp, K. G.; Strothkamp, R. E. Fluorescence Measurements of Ethidium Binding to DNA. *J. Chem. Educ.* **1994**, *71*, 77.

(53) Wu, H.; Yuan, J.; Bai, Y.; Pan, G.; Wang, H.; Shu, X. Synthesis, Structure, DNA-binding Properties and Antioxidant Activity of a Nickel (II) Complex with bis-(N-allylbenzimidazol-2-ylmethyl) benzylamine. *J. Photochem. Photobiol., B* **2012**, *107*, 65−72.

(54) Parsekar, S. U.; Singh, M.; Mishra, D. P.; Antharjanam, P. K. S.; Koley, A. P.; Kumar, M. Efficient hydrolytic cleavage of DNA and antiproliferative effect on human cancer cells by two dinuclear Cu(II) complexes containing a carbohydrazone ligand and 1,10-phenanthroline as a coligand. *J. Biol. Inorg. Chem.* **2019**, *24*, 343−363.

(55) Dhar, S.; Reddy, P. A.; Chakravarty, A. R. Intramolecular Nucleophilic Activation Promoting Efficient Hydrolytic Cleavage of DNA by (aqua)bis-(dipyridoquinoxaline)copper(II) Complex. *Dalton Trans.* **2004**, 697−698.

(56) Rajalakshmi, S.; Weyhermüller, T.; Freddy, A. J.; Vasanthi, H. R.; Nair, B. U. Anomalous Behavior of Pentacoordinate Copper Complexes of Dimethylphenanthroline and Derivatives of Terpyridine Ligands: Studies on DNA Binding, Cleavage and Apoptotic activity. *Eur. J. Med. Chem.* **2011**, *46*, 608−617.

(57) Jayamani, A.; Thamilarasan, V.; Ganesan, V.; Sengottuvelan, N. Structural, Electrochemical, DNA Binding and Cleavage Properties of Nickel (II) Complex [Ni (H_2biim)$_2$ (H_2O)$_2$]$^{2+}$ of 2, 2'-Biimidazole. *Bull. Korean Chem. Soc.* **2013**, *34*, 3695−3702.

(58) Hemnani, T.; Parihar, M. S. Reactive Oxygen Species and Oxidative DNA Damage. *Indian J. Physiol. Pharmacol.* **1998**, *42*, 440−452.

(59) Zhao, Y.; Zhu, J.; He, W.; Yang, Z.; Zhu, Y.; Li, Y.; Zhang, J.; Guo, Z. Oxidative DNA Cleavage Promoted by Multinuclear Copper Complexes: Activity Dependence on the Complex Structure. *Chem.—Eur. J.* **2006**, *12*, 6621−6629.

(60) Samari, F.; Hemmateenejad, B.; Shamsipur, M.; Rashidi, M.; Samouei, H. Affinity of Two Novel Five-coordinated Anticancer Pt(II) Complexes to Human and Bovine Serum Albumins: a Spectroscopic Approach. *Inorg. Chem.* **2012**, *51*, 3454−3464.

(61) Bijelic, A.; Theiner, S.; Keppler, B. K.; Rompel, A. X-ray Structure Analysis of Indazolium *trans*-[Tetrachlorobis(1*H*-indazole)ruthenate-(III)] (KP1019) Bound to Human Serum Albumin Reveals Two Ruthenium Binding Sites and Provides Insights into the Drug Binding Mechanism. *J. Med. Chem.* **2016**, *59*, 5894−5903.

(62) Hummer, A. A.; Bartel, C.; Arion, V. B.; Jakupec, M. A.; Meyer-Klaucke, W.; Geraki, T.; Quinn, P. D.; Mijovilovich, A.; Keppler, B. K.; Rompel, A. X-ray Absorption Spectroscopy of an Investigational Anticancer Gallium(III) Drug: Interaction with Serum Proteins,

https://doi.org/10.1021/acsomega.3c01853
ACS Omega 2023, 8, 21948−21968

Elemental Distribution Pattern, and Coordination of the Compound in Tissue. *J. Med. Chem.* **2012**, *55*, 5601−5613.
(63) Wang, S.; Liu, S.; Zhang, Y.; He, J.; Coy, D. H.; Sun, L. Human Serum Albumin (HSA) and its Applications as a Drug Delivery Vehicle. *Health Sci. J.* **2020**, *14*, 698.
(64) Munteanu, A. C.; Badea, M.; Olar, R.; Silvestro, L.; Mihaila, M.; Brasoveanu, L. I.; Musat, M. G.; Andries, A.; Uivarosi, V. Cytotoxicity Studies, DNA Interaction and Protein Binding of new Al (III), Ga (III) and In (III) Complexes with 5-hydroxyflavone. *Appl. Organomet. Chem.* **2018**, *32*, No. e4579.
(65) Shahabadi, N.; Fili, S. M.; Kashanian, S. Human Serum Albumin Interaction Studies of a New Copper(II) Complex Containing Ceftobiprole Drug Using Molecular Modeling and Multispectroscopic Methods. *J. Coord. Chem.* **2018**, *71*, 329−341.
(66) Cui, F. L.; Qin, L. X.; Li, F.; Luo, H. X. Synchronous Fluorescence Determination and Molecular Modeling of 5-Amino-salicylic acid (5-ASA) Interacted with Human Serum Albumin. *J. Mol. Model.* **2008**, *14*, 1111−1117.
(67) Gan, Q.; Fu, X.; Chen, W.; Xiong, Y.; Fu, Y.; Chen, S.; Le, X. Synthesis, DNA/HSA Interaction, Spectroscopic Studies and in vitro Cytotoxicity of a new Mixed Ligand Cu(II) Complex. *J. Fluoresc.* **2016**, *26*, 905−918.
(68) Rahman, S.; Rehman, M. T.; Rabbani, G.; Khan, P.; AlAjmi, M. F.; Hassan, M.; Muteeb, G.; Kim, J. Insight of the interaction between 2,4-thiazolidinedione and human serum albumin: A spectroscopic, thermodynamic and molecular docking study. *Int. J. Mol. Sci.* **2019**, *20*, 2727.
(69) Sekar, R. B.; Periasamy, A. Fluorescence Resonance Energy Transfer (FRET) Microscopy Imaging of Live Cell Protein Localizations. *J. Cell Biol.* **2003**, *160*, 629−633.
(70) *FRET-Forster Resonance Energy Transfer: From Theory to Applications*; Hildebrandt, N., Medintz, I. L., Eds.; Wiley-VCH Verlag GmbH, 2014.
(71) Hussain, A.; AlAjmi, M. F.; Rehman, M. T.; Amir, S.; Husain, F. M.; Alsalme, A.; Siddiqui, M. A.; AlKhedhairy, A. A.; Khan, R. A. Copper (II) Complexes as Potential Anticancer and Nonsteroidal Anti-inflammatory Agents: In vitro and In vivo Studies. *Sci. Rep.* **2019**, *9*, 5237−5317.
(72) Kathiresan, S.; Mugesh, S.; Annaraj, J.; Murugan, M. Mixed-ligand Copper (II) Schiff base Complexes: the Vital Role of Co-ligands in DNA/Protein Interactions and Cytotoxicity. *New J. Chem.* **2017**, *41*, 1267−1283.
(73) Meerloo, J. V.; Kaspers, G. J.; Cloos, J. Cell Sensitivity Assays: The MTT Assay. *Methods Mol. Biol.* **2011**, *731*, 237−245.
(74) Cooper, G. M.; Hausman, R. E. *The Cell: A molecular approach*, 2nd ed.; Sinauer Associates: Sunderland, MA, 2000.
(75) Allen, S.; Sotos, J.; Sylte, M. J.; Czuprynski, C. J. Use of Hoechst 33342 Staining to Detect Apoptotic Changes in Bovine Mononuclear Phagocytes Infected with Mycobacterium Avium subsp. Paratuberculosis. *Clin. Diagn. Lab. Immunol.* **2001**, *8*, 460−464.
(76) Elmore, S. Apoptosis: A Review of Programmed Cell Death. *Toxicol. Pathol.* **2007**, *35*, 495−516.
(77) Ramakrishnan, S.; Rajendiran, V.; Palaniandavar, M.; Periasamy, V. S.; Srinag, B. S.; Krishnamurthy, H.; Akbarsha, M. A. Induction of Cell Death by Ternary Copper(II) Complexes of L-tyrosine and Diimines: Role of Coligands on DNA Binding and Cleavage and Anticancer Activity. *Inorg. Chem.* **2009**, *48*, 1309−1322.
(78) Anbu, S.; Ravishankaran, R.; Karande, A. A.; Kandaswamy, M. DNA Targeting Polyaza Macrobicyclic Dizinc(II) Complexes Promoting High in vitro Caspase Dependent Anti-proliferative Activity Against Human Carcinoma Cancer Cells. *Dalton Trans.* **2012**, *41*, 12970−12983.
(79) Zahedifard, M.; Lafta Faraj, F.; Paydar, M.; Yeng Looi, C.; Hajrezaei, M.; Hasanpourghadi, M.; Kamalidehghan, B.; Abdul Majid, N.; Mohd Ali, H.; Ameen Abdulla, M. Synthesis, Characterization and Apoptotic Activity of Quinazolinone Schiff Base Derivatives Toward MCF-7 Cells via Intrinsic and Extrinsic Apoptosis Pathways. *Sci. Rep.* **2015**, *5*, 11544−11617.
(80) Hajrezaie, M.; Paydar, M.; Zorofchian Moghadamtousi, S.; Hassandarvish, P.; Gwaram, N. S.; Zahedifard, M.; Rouhollahi, E.; Karimian, H.; Looi, C. Y.; Ali, H. M.; Abdul Majid, N.; Abdulla, M. A. A Schiff Base-derived Copper(II) Complex is a Potent Inducer of Apoptosis in Colon Cancer Cells by Activating the Intrinsic Pathway. *Sci. World J.* **2014**, *2014*, 1−12.
(81) Koley, M. K.; Duraipandy, N.; Kiran, M. S.; Varghese, B.; Manoharan, P. T.; Koley, A. P. DNA Binding and Cytotoxicity of Some Cu(II)/Zn(II) Complexes Containing a Carbohydrazone Schiff Base Ligand Along with 1, 10-Phenanthroline as a Coligand. *Inorg. Chim. Acta* **2017**, *466*, 538−550.
(82) Koley, M. K.; Parsekar, S. U.; Duraipandy, N.; Kiran, M. S.; Varghese, B.; Manoharan, P. T.; Koley, A. P. DNA Binding and Cytotoxicity of Two Cu(II) Complexes Containing a Schiff Base Ligand Along with 1, 10-Phenanthroline or Imidazole as a Coligand. *Inorg. Chim. Acta* **2018**, *478*, 211−221.
(83) Budihardjo, I.; Oliver, H.; Lutter, M.; Luo, X.; Wang, X. Biochemical Pathways of Caspase Activation During Apoptosis. *Annu. Rev. Cell Dev. Biol.* **1999**, *15*, 269−290.
(84) Desouza, M.; Gunning, P. W.; Stehn, J. R. The Actin Cytoskeleton as a Sensor and Mediator of Apoptosis. *Bioarchitecture* **2012**, *2*, 75−87.

https://doi.org/10.1021/acsomega.3c01853
ACS Omega 2023, 8, 21948−21968